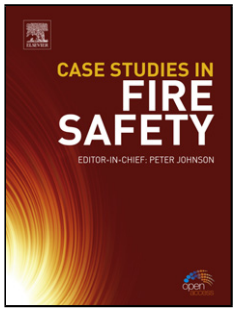

Title: Further study of the hydrogen embrittlement of martensitic advanced high strength steel in simulated auto service conditions

Authors: Jeffrey Venezuela, Jethro Blanch, Azmir Zulkiply, Qinglong Liu, Qingjun Zhou, Mingxing Zhang, Andrej Atrens

PII: S0010-938X(17)30065-3
DOI: https://doi.org/10.1016/j.corsci.2018.02.037
Reference: CS 7394

To appear in:

Received date: 13-1-2017
Revised date: 8-2-2018
Accepted date: 19-2-2018

Please cite this article as: Jeffrey Venezuela, Jethro Blanch, Azmir Zulkiply, Qinglong Liu, Qingjun Zhou, Mingxing Zhang, Andrej Atrens, Further study of the hydrogen embrittlement of martensitic advanced high strength steel in simulated auto service conditions, Corrosion Science https://doi.org/10.1016/j.corsci.2018.02.037

Further study of the hydrogen embrittlement of martensitic advanced high strength steel in simulated auto service conditions

Jeffrey Venezuela[a], Jethro Blanch[a], Azmir Zulkiply[a], Qinglong Liu[a], Qingjun Zhou[b,*], Mingxing Zhang[a], Andrej Atrens[a,*]

[a] The University of Queensland, Division of Materials, School of Mining and Mechanical Engineering, St. Lucia, 4072 Australia
[*] Corresponding author, andrejs.atrens@uq.edu.au, +61 7 3365 3748, zhouqingjun@baosteel.com, +86 21 26641807
[b] Baoshan Iron & Steel Co., Ltd, Research Institute, Shanghai, 201900,China

Highlights

- Susceptibility increased at increasingly negative potentials and at lower pH in 3.5% NaCl
- Susceptibility increased at high charging potentials in 0.1 M NaOH at substantial stress rates.
- The hydrogen influence was manifested by reduced ductility and brittle fracture features

ABSTRACT

This work examines the influence of hydrogen on the mechanical and fracture properties of martensitic advanced high-strength steels under conditions relevant to automotive service: (i) in 3.5 wt% NaCl at different cathodic potentials, (ii) in acidified 3.5 wt% NaCl and (iii) at substantial stress rates. The hydrogen embrittlement susceptibility of the steels increases at (i) increasingly negative potentials and at lower pH in 3.5 wt% NaCl, and (ii) at high charging potentials in 0.1 M NaOH at substantial stress rates. The hydrogen influence is manifested by a reduction in ductility, and the presence of brittle features on the fracture surface.

Keywords: A. steel; B. SEM; C. hydrogen embrittlement

1. Introduction

Martensitic advanced high-strength steels (MS-AHSS) are attracting attention for the manufacture of lightweight, crashworthy cars [1-3]. MS-AHSS have good strengths, ranging 950 to 1700 MPa, are inexpensive to manufacture, but exhibit limited ductility and formability [4, 5]. MS-AHSS are used to make automotive body-in-white (BIW) components such as (i) bumper beams and reinforcements, (ii) door intrusion beams and reinforcements, (iii) windscreen upright reinforcements, and (iv) B-pillar reinforcements [1, 6-8].

Hydrogen embrittlement (HE) occurs in steels, such as in conventional high-strength steels [9-24], advanced high-strength steels [25-39], and medium-strength steels [40-49]. HE occurs when the load-bearing steel interacts with a critical amount of hydrogen. HE can result in (i) a reduction of mechanical strength, toughness and ductility, together with (ii) subcritical crack growth [50, 51]. Alternatively, HE can cause some reduction of ductility without an appreciable decrease in yield and tensile strength [52], and without sub-critical crack growth.

Automotive steels may be subject to corrosion in automobile service. A marine environment is a common environment that causes aggressive corrosion of steels in the auto body [53]. Similar aggressive corrosion occurs for auto bodies due to de-icing salts used in snowy climates. Hydrogen may be produced by the corrosion, may diffuse into the stress-bearing steel auto component, and could conceivably cause hydrogen delayed fractures [54].

During accidents, car components are subjected to impact stresses at high-applied stress rates. Adequate toughness in automotive steels is needed so that the component fails by a ductile mode rather than fractures. Any factor that could lower the toughness of an automotive structure, such as hydrogen, requires to be understood by car manufacturers.

This current research builds on our previous study, which studied the HE susceptibility of automotive MS-AHSS in simulated service conditions, using the linearly increasing stress test (LIST) and conventional tensile tests [27]. The LIST [55] has been widely used to study hydrogen embrittlement (HE) and stress corrosion cracking (SCC) [9, 10, 14, 42, 56-62]. Our previous work [27] studied four grades of MS-AHSS using LIST at the open circuit potential, E_{corr}, and at the zinc potential, E_{Zn}, equivalent to -950 $mV_{Ag/AgCl}$ (-752 mV_{SHE}), in 3.5% NaCl and at different stress rates. There was minimal HE susceptibility in these MS-AHSS at both E_{corr} and E_{Zn}, and at all stress rates; partly due to the low hydrogen concentrations under these hydrogen-charging conditions.

However, it is possible that HE in these steels could occur at higher cathodic potentials where a greater hydrogen fugacity is expected [63]. In addition, it is known that the

hydrogen equilibrium potential decreases with decreasing pH [64], so that there is more hydrogen evolution during corrosion in acidic solutions. This means that a decrease in pH can increase the corrosion rate of steels [53], and would also increase the amount of hydrogen produced during corrosion. Also, the presence of NaCl would further add to the aggressiveness of corrosion in acidic solutions.

Acidified NaCl solutions occur during crevice corrosion and pitting corrosion. The pH can decrease to below pH 2 inside a crevice and a corroding pit, in a NaCl solution [65]. Thus tests on steels immersed in acidified 3.5% NaCl are relevant to understand the sensitivity of MS-AHSS to the conditions present in crevice corrosion and pitting corrosion.

In each case, as in our prior research [25, 27, 39], cathodic pre-charging was carried out for 24 h before the commencement of any testing to ensure that (i) there was a stable surface condition at the charging surface, and (ii) the hydrogen concentration was uniform throughout the specimen. Our prior research using permeation experiments [27-29, 36], indicated that long-term hydrogen pre-charging was required to ensure the reduction of the initial surface oxides to a steady state condition, for which the permeation current density was stable. Furthermore, modelling of the hydrogen concentration using the diffusion coefficients measured in the permeation experiments indicated that the hydrogen concentration was a constant throughout the specimens used for these long term charging conditions [27-29, 36].

Our previous study used tensile tests to study the influence of a substantial-applied stress rate on the HE susceptibility of MS-AHSS under conditions of internal hydrogen embrittlement (IHE) [27]. IHE refers to HE in the absence of hydrogen charging [66]. The hydrogen is already inside the steel, i.e. the hydrogen may have entered the steel during the processing or fabrication steps or during previous service corrosion. IHE was evaluated by mechanical tests on specimens in the absence of hydrogen charging [27]. Smooth tensile specimens were hydrogen charged in tension in the LIST apparatus, dismounted, and then subjected to a tensile test using a universal testing machine (UTM) within a short time after the end of hydrogen charging. The results did show negligible hydrogen influence on the mechanical properties of MS-AHSS, even though modelling indicated that most of the hydrogen remained in the steel.

In contrast, external hydrogen embrittlement (EHE), also known as hydrogen environment embrittlement (HEE), results from exposure to a hydrogen-bearing environment [67]. For hydrogen gas, hydrogen is believed to enter the metal via the surface adsorption of diatomic hydrogen, followed by absorption in the lattice after dissociation into the

monoatomic form. EHE is evaluated by mechanical tests in the presence of a hydrogen environment.

Past research has noted several similarities and differences between IHE and EHE [68]. Both processes need a critical level of stress and a critical hydrogen concentration. It is possible that the MS-AHSS may behave differently when evaluated under EHE conditions.

The present paper adds to the knowledge of the relevance of the HE to MS-AHSS in automobile service. The specific issues addressed by this work were as follows:

1. the HE susceptibility of MS-AHSS in 3.5wt% NaCl at -950 $mV_{Ag/AgCl}$ (-752 mV_{SHE}) and -1050 $mV_{Ag/AgCl}$ (-852 mV_{SHE}), and the measurement of the hydrogen concentrations in the steels at these potentials,
2. the HE susceptibility of MS-AHSS in pH-modified 3.5wt% NaCl, to assess the HE susceptibility of MS-AHSS during pit corrosion or crevice corrosion, and
3. the EHE of MS-AHSS under a substantial loading rate that is relevant to a crash situation.

2. Experimental methods

2.1. Steels, electrolytes, and apparatus

The test materials were four grades of commercial MS-AHSS; namely MS980, MS1180, MS1300 and MS1500. The steels were from commercial production, and were supplied as flat rolled sheets with the chemical composition and the mechanical properties as presented in Table 1. The chemical composition was determined by an independent laboratory (Spectrometer Services Pty Ltd, Coberg, Vic), whilst the mechanical properties were provided by the steel supplier. The microstructure of these steels consisted of a combination of mainly martensite and some ferrite [25], with proportions as listed in Table 1.

The LIST and tensile test specimens were machined using a water jet cutter to the dimensions shown in Fig 1. The long direction of each specimen was parallel to the rolling direction. The specimens were mechanically ground using SiC paper (i.e. 320, 600 and 1200 grit), rinsed with ethanol, and blow-dried. The specimen thicknesses were: (i) 1.5 mm for MS980, (ii) 1.70 mm for MS1180, (iii) 1.20 mm for MS1300, and (iv) 1.18 mm for MS1500.

All solutions, i.e. 3.5wt% NaCl, 0.1 M NaOH, and 0.1 M HCl, were prepared using analytic grade chemicals and deionised water. The pH modifiers were analytic grade (i) 32wt% hydrochloric acid (HCl) and (ii) sodium hydroxide pellets.

Electrochemical hydrogen charging used a three-electrode apparatus. The working electrode was the steel specimen. The reference electrode was either an Ag/AgCl/sat KCl reference electrode when hydrogen charging in 3.5wt% NaCl, or a Hg/HgO/20wt% KOH reference electrode when hydrogen charging in 0.1 M NaOH. The counter electrode was graphite, because our previous work indicated that a graphite electrode was inert with respect to electrolytic hydrogen charging, whereas a platinum counter electrode caused a smaller amount of hydrogen to be absorbed by the steel because of the plating of platinum onto the steel working electrode [27].

The Linearly Increasing Stress Test (LIST) has been described previously [25-27, 55]. The LIST subjects the specimen, exposed to the environment of interest, to a linearly increasing stress until specimen fracture. The LIST is equivalent to a load controlled slow strain rate test (SSRT), that is considerably quicker than the SSRT, because specimen fracture occurs much earlier, e.g. for a specimen in air, fracture occurs at the maximum load when the specimen becomes mechanically unstable and fractures; and the specimen fractures when the sub-critical crack reaches a critical size for testing in an environment causing sub-critical cracking [58]. The tensile strength, σ_F, and yield and threshold stress, σ_{TH}, were determined using the potential drop method. The reduction in area, R_A, was obtained by measuring the projected area of the fracture surface. The HE susceptibility index, I, was evaluated as follows [25]:

$$I = \frac{R_{A,air} - R_{A,H}}{R_{A,air}} 100\% \quad (1)$$

where $R_{A,air}$ is the reduction in area in air, and $R_{A,H}$ is the reduction in area in the hydrogen charging environment. The value of I can range from 0% to 100%, from no HE susceptibility to maximum HE susceptibility due to the complete absence of plastic strain during failure.

The conventional tensile tests were conducted using an Instron 4505 universal testing machine (UTM) following the ASTM E-8 standard.

After each mechanical test (i.e. LIST or tensile test), the fractured specimen was subjected to fracture analysis. At the end of a test that involved electrochemical charging, the fractured specimen was immediately removed from the charging electrolyte to prevent corrosion of the fracture surface. The specimen was rinsed in distilled water, blow-dried, immersed in EDTA solution for 5 minutes, rinsed with ethanol and blow-dried. Each specimen was cut to an appropriate size using an alumina saw, ultrasonically cleaned in a 4wt% alconox solution for 30 minutes, rinsed in deionized water, and blow-dried. The

specimen was mounted on an aluminium stub using a conductive carbon tape, and examined using a scanning electron microscope (JEOL 6610 SEM).

2.2. LISTs in 3.5wt% NaCl with applied potentials

2.2.1. E_{Zn}

Four grades of MS-AHSS (i.e. MS980, MS1180, MS1300 and MS1500) were studied. The LIST specimen was fixed into the solution chamber and the chamber was mounted on the LIST apparatus. An initial tensile stress equivalent to 20% of the nominal yield stress was applied to the specimen. The 3.5wt% NaCl charging solution was poured into the chamber, the appropriate reference and counter electrodes were inserted, and a cathodic potential equivalent to E_{Zn} (-950 $mV_{Hg/HgO}$ (-752 mV_{SHE})) was applied to the specimen for 24 hours to attain hydrogen saturation throughout the specimen, as verified by our prior modelling of the hydrogen profile in the specimen [27]. At the end of the charging period, the LIST commenced. An applied stress rate equivalent to the 3 revolutions/h (rph) motor was applied on the specimen. The stress rate was determined from the cross-sectional area of the specimen and the speed of the servomotor used (e.g. 3 or 30 rph motor), and is provided with the results in the appropriate table.

2.2.2. -1050 $mV_{Ag/AgCl}$

The two strongest grades of MS-AHSS; namely, MS1300 and MS1500, were used in these tests as these showed the most hydrogen sensitivity [25]. The test procedure was as described in section 2.2.1, except that (i) the cathodic charging potential applied was -1050 $mV_{Ag/AgCl}$ (-852 mV_{SHE}) and (ii) two stress rates were studied corresponding to the 30 (0.08 MPa s^{-1}) and 3 rph (0.008 MPa s^{-1}) motors.

2.3. Permeation tests

The permeation tests were conducted to determine (i) the hydrogen concentrations in the MS1300 and MS1500 during charging in the 3.5wt% NaCl at the different potentials, and (ii) the effective hydrogen diffusion coefficients. The tests were performed as described previously [27] including precharging for 24 h at -1050 $mV_{Ag/AgCl}$ in 3.5wt% NaCl. There were attempts to do charging at potentials more negative than -1050 $mV_{Ag/AgCl}$ (-852 mV_{SHE}). However, beyond -1050 $mV_{Ag/AgCl}$ (-852 mV_{SHE}), the toxic gas chlorine was evolved, probably due to the oxidation of chloride ions at the counter electrode; and thus the tests were discontinued. The specimen thicknesses were 1.13 mm for MS1300 specimens and 1.09 mm for MS1500 specimens.

The permeation transients were as follows: (i) successive decay transients from -1050 to -950, then -950 to -850 $mV_{Ag/AgCl}$; (ii) successive rise transients from -850 to -950, then -950 to -1050 $mV_{Ag/AgCl}$; and (iii) full decay from -1050 $mV_{Ag/AgCl}$ to the open cell potential.

The permeation tests were analysed as previously [27]. Permeation transients were fitted with the theoretical curves derived from the appropriate mathematical model that describes a rise or a decay transient; expressed as follows [69]:

Rise: $$\frac{i_p - i_p^0}{i_p^\infty - i_p} = \frac{2L}{\sqrt{\pi D_{eff} t}} \sum_{n=0}^{\infty} \exp\left(-\frac{(2n+1)^2 L^2}{4 D_{eff} t}\right) \quad (2)$$

Decay: $$\frac{i_p - i_p^0}{i_p^\infty - i_p^0} = 1 - \frac{2L}{\sqrt{\pi D_{eff} t}} \sum_{n=0}^{\infty} \exp\left(-\frac{(2n+1)^2 L^2}{4 D_{eff} t}\right) \quad (3)$$

where i_p is the permeation current during a build-up or decay transient at time, t, D_{eff} is the effective diffusion coefficient, L is the specimen thickness, i_p^0 is the initial permeation current density, and i_p^∞ is the steady-state permeation current density at that applied potential. The fitted curve yielded the effective hydrogen diffusion coefficient in the steel, D_{eff}. The subsurface concentration of hydrogen, C_H, at the entry side of the steel during charging in the permeation test was evaluated from [69, 70]:

$$C_H = \frac{i_\infty L}{F D_{eff}} \quad (4)$$

where i_∞ is the steady state permeation current density, L is the steel membrane thickness, and F is the Faraday constant (96485 C mol^{-1}).

2.4. LISTs in pH-modified 3.5wt% NaCl

Only MS1500, which has the highest HE susceptibility, was used in this test. LISTs were performed in pH-modified 3.5wt% NaCl at the open cell potential, E_{corr}, at commencing pH values of 1, 3, 5 and 9. The as-prepared or unmodified 3.5wt% NaCl solution had a pH value of 7.4. The pH was modified using analytic grade (i) 32wt% hydrochloric acid (HCl) and (ii) sodium hydroxide pellets. The LIST specimen was placed in the charging cell together with the charging solution, and pre-charged for 24 h at 20% yield stress. The test was performed at a stress rate corresponding to the 30 rph (0.08 MPa s^{-1}) motor. Another test was done in 0.1 M HCl solution with pH 1.

2.5. Tensile tests

Tensile tests were conducted in (i) air; (ii) in 0.1M NaOH whilst hydrogen charging at -1100 $mV_{Hg/HgO}$ (-1002 mV_{SHE}), -1400 $mV_{Hg/HgO}$ (-1302 mV_{SHE}) and -1700 $mV_{Hg/HgO}$ (-1602 mV_{SHE}); and (iii) at E_{Zn} equivalent to -950 $mV_{Ag/AgCl}$ (-752 mV_{SHE}) in 3.5wt% NaCl. The same charging chamber used in the LIST was adopted for the tensile test. The specimen was mounted in the charging chamber then connected to the UTM. The charging solution was poured in the chamber, and the electrodes were inserted. A pre-test load was applied on the specimen during charging equivalent to 20% of the nominal yield stress of the steel. The appropriate charging potential was applied on the specimen for 24 hours. At the end of the hydrogen charging step, the tensile test commenced. The applied strain rate was 0.015 mm/mm/min. This deformation rate was equivalent to 50 MPa s^{-1} in the initial elastic part of the test, which was about six hundred times faster than the stress rate of 0.080 MPa s^{-1} using the 30 rph LIST motor. Due to the absence of a yield plateau, the yield stress, σ_y, was obtained at the 0.2% offset strain. The ultimate tensile stress, σ_f, was obtained at the point of maximum load, whilst ductility was measured from the % reduction in area, R_A.

The tensile test was carried out under strain control compared with the LISTs, which are load controlled. Thus the specimen in a LIST necks and fractures at the ultimate tensile strength, whereas there is considerable additional deformation in the tensile test after necking at the maximum load.

An extensometer could not be used in these tensile tests since the charging cell prevented mounting the extensometer on the specimen. The extensions were measured from the displacement of the crosshead. Experience has indicated that, when extension is taken from the crosshead displacement, the gauge length is equivalent to the distance between grips. In these tests, the distance between grips was about 75 mm.

3.0 Results

3.1. LIST in 3.5wt% NaCl solution with applied potentials

Fig. 2 shows typical LIST potential-drop data, consisting of plots of the potential drop across the specimen versus the applied stress. The yield or threshold stress, σ_{TH}, was determined as the transition stress corresponding to the significant increase in the slope. The fracture stress, σ_F, was determined from the maximum load. Table 2 presents a summary of the measured values of σ_{TH}, the tensile fracture stress, σ_F, the reduction in area, R_A, and the hydrogen embrittlement index, I, obtained from the LISTs in air, and in 3.5wt% NaCl at the stated charging potentials and stress rates.

The values of σ_{TH} and σ_F for the four MS-AHSS evaluated using LISTs in air were similar to the values obtained from the steel supplier as listed in Table 1.

3.1.1. E_{Zn} and -1050 $mV_{Ag/AgCl}$

Table 2 indicates that, for the four steels tested in the LIST in 3.5wt% NaCl at E_{Zn} at the slowest stress rate (3 rph), the values of σ_{TH} and σ_F were similar to the values measured in air. However, there were changes in ductility that were reflected in the corresponding I value. MS980, MS1180 and MS1300 exhibited little change in ductility and had low values I; whilst MS1500 showed a significant decrease in ductility as indicated by the higher I value.

At the more cathodic potential of -1050 $mV_{Ag/AgCl}$ (-852 mV_{SHE}), the values of σ_{TH} and σ_F of MS1300 and MS1500 were again similar to the values measured in air. However, the two steels showed considerable HE susceptibility, as indicated by a decrease in the value of R_A and an increase in the value of I. MS1500 exhibited higher I values than MS1300. Furthermore, the MS1300 and MS1500 both exhibited higher I values at the lower applied stress rate.

3.1.2. Fracture characteristics

There were two types of fractures: (i) cup-cone fracture and (ii) shear fracture. Representative images of these two fracture modes are shown in Fig. 3.

Cup-cone fracture was typically accompanied by considerable necking, and indicated ductile behaviour. There was cup-cone fracture in the specimens tested (i) in air, or (ii) for the steels with minimal hydrogen influence as indicated by low I values (e.g. MS980-Ezn-3 and MS1300-E-30). The typical features present in the cup-cone fracture are shown in Fig 4: (i) the central fracture region (‘C’) and (ii) the shear lip region (‘S’). The arrows indicate crack propagation. The typical fracture morphologies in the ‘C’ region were micro-void

coalescence (MVC) dimples, as shown in Fig 4b. In the 'S' region there were shallow parabolic MVC dimples, as shown in Fig 4c. In some of the specimens, such as MS1500-E-30, surface cracks were present in the neck region of the cup-cone fracture, but there were, in no case, cracks in the uniformly deformed part of the specimen.

Shear fracture was an indication of more macroscopically-brittle behaviour. This fracture mode was also accompanied by some necking and surface cracks near the crack lip, but there were, in no case, cracks in the uniformly deformed part of the specimen away from the final fracture. The shear fracture occurred for steels with a substantial hydrogen influence that correlated with higher *I* values (e.g. MS1500-E-3, MS1500-Ezn-30 and MS1300-E-3).

Details of the shear fracture are shown in Fig. 5. Three fracture zones were identified: (i) fracture initiation ('I'); (ii) fracture propagation ('P'); and the (iii) final fracture ('F') region. The 'I' region commonly possessed brittle features such as a mix of intergranular, transgranular and quasi-cleavage fractures, as shown in Fig 5b. The 'P' region consisted of shallow, shear MVC dimples, as shown in Fig 5c. The fracture propagated typically at an angle of 45^{o} with respect to the direction of the tensile load. The 'F' zone, shown in Fig 5d, possessed brittle features that were similar to those observed in the fracture initiation zone.

3.2. Permeation tests

Fig. 6a shows the transient loop conducted during the permeation test. Fig. 6b shows a typical build-up or rise transient curve fitted with the theoretical curve derived using the appropriate mathematical model [27, 63]. Table 3 presents the steady state permeation current, i_{∞}, the effective hydrogen diffusion coefficient, $D_{\text{eff,}}$ and the subsurface hydrogen concentration, C_{H}, for MS1300 and MS1500.

The values of C_{H} increased with increasingly negative charging potentials. The values of C_{H} ranged from 0.024 to 0.137 µg g^{-1} in MS1300, and 0.014 to 0.115 µg g^{-1} in MS1500, for a potential range of -850 (-652 mV_{SHE}) to -1050 $mV_{Ag/AgCl}$ (-852 mV_{SHE}). The calculated mean D_{eff} in MS1300 was 12.3 x 10^{-7} cm^2 s^{-1}, which was slightly lower than that of MS1500 at 13.2 x 10^{-7} cm^2 s^{-1}.

3.3. LIST in pH-modified 3.5wt% NaCl

3.3.1. LIST results

Table 4 presents the LIST results for MS1500 tested in (i) different pH-modified 3.5wt% NaCl solution and (ii) NaCl-free pH 1 HCl solution at an applied stress rate of 0.08 MPa s^{-1} and at E_{corr}. The specimens immersed in the pH 5, 7 and 9 NaCl solutions formed a visible red precipitate, attributed to rusting of the steel to form ferric oxide/hydroxide. Some

of the precipitates dislodged from the specimen and settled at the bottom of the charging chamber. In the pH 1 and 3 NaCl solutions, there were no visible corrosion products at the specimen surface. However, there was a considerable amount of gas bubbles at the surface of the steel immersed in the pH 1 solutions, attributed to hydrogen evolution at the specimen surface as the cathodic partial reaction.

In most of the tests, both σ_{TH} and σ_F of MS1500 had values similar to the values obtained in air. In contrast, each steel immersed in the two pH 1 solutions (i.e. MS1500-S-pH1 and MS1500-pH1) had a significant reduction in both σ_{TH} and σ_F. The measured σ_{TH} and σ_F values of MS1500 in these two tests were almost similar, although there were significant differences in the R_A and I values.

Table 4 indicates that, as the pH of the NaCl solution decreased, the ductility of MS1500 decreased, and consequently the I value increased. MS1500 immersed in the pH 1 NaCl solution had the highest I value of 84. The I values of MS1500 at the higher pH NaCl solutions; i.e. from pH 3 to pH 7, were significantly lower than that measured in pH 1, and decreased from 26 to 2. At pH 9, the I value of MS1500 (I = 8) was slightly higher than in pH 7 (~2).

The ductility of MS1500 was appreciably lower in the NaCl pH 1 solution than in the NaCl-free HCl solution at the same pH of 1. Consequently, the I value was higher for MS1500 immersed in the pH 1 3.5wt% NaCl. There was more than a 50% increase in the I value from MS1500-pH1 (I = 54) to MS1500-S-pH1 (I = 84).

3.3.2 Fracture characteristics in pH-modified 3.5wt% NaCl

Table 4 summarizes the fracture characteristics of MS1500 in the acidified 3.5wt% NaCl. Similar to previous results, MS-AHSS exhibited two fractures modes under these charging conditions: (i) ductile, cup-cone and (ii) brittle, shear failure.

The steels tested in air, and immersed in the pH 5, 7 and 9 3.5wt% NaCl solutions underwent ductile, cup-cone fracture accompanied by considerable necking. Typical SEM images of these fractures are presented in Fig. 7.

The steels immersed in both pH 1 solutions (i.e. acidified 3.5wt% NaCl pH 1 and the NaCl-free HCl solution) exhibited shear fracture. Fig. 8 presents a comparison of these fractures viewed from the transverse side. In the pH 1 3.5wt% NaCl, the shear fracture in MS1500-S-pH1 was quite sharp, and without visible necking. In the NaCl-free pH 1 HCl, the shear fracture in MS1500-pH1 occurred with some plastic deformation (i.e. some necking).

Fig. 9a and 9b shows the details of the shear fracture for the two tests in the pH 1 solutions. The two fractures possessed typical shear fracture features as described previously: (i) 'I', (ii) 'P', and (iii) 'F' regions. The 'P' region of MS1500-S-pH1 was significantly smoother than that of MS1500-pH1. Fig 9c and 9d present a magnified view of the P region. MS1500-S-pH1 consisted of shallow and fine MVC shear dimples; whilst MS1500-pH1 possessed coarse MVC dimples. The MVC dimples in MS1500-S-pH1 were about 4 to 8 times smaller than MS1500-pH1.

Fig. 10 presents the fracture mode for MS1500 immersed in the pH 3 3.5wt% NaCl solution at a stress rate of 0.080 MPa s^{-1}; this fracture can be considered mixed cup-cone and shear fracture. Fig. 10a presents the top view of the fracture. From this view, the fracture propagation history and the features are characteristic of ductile, cup-cone fracture; i.e. (i) a central, fracture nucleation region; and (ii) a shear lip region. There were signs of necking. The size of the central region was unusually small, and the shear lip region appears blocky and jagged. In contrast, the view from the transverse side shows: (i) a coarse, jagged fracture, as shown in Fig. 10b; and (ii) surface cracks at 45^o indicative of shear fracture, as shown in Fig. 10c. Both of these features suggest some brittle behaviour.

3.4. Tensile tests

3.4.1. 0.1 M NaOH and 3.5wt% NaCl

Fig. 11 shows the typical stress-strain curves obtained from the tensile tests. The tensile tests in solution were carried out after 24 h hydrogen pre-charging and had simultaneous hydrogen charging during the tensile tests. Table 5 presents the values σ_y, σ_F, R_A, and I of the four MS-AHSS charged at (i) different potentials in 0.1 M NaOH and at (ii) E_{Zn} in 3.5wt% NaCl. In a majority of the tests in 0.1 M NaOH, the σ_y and σ_F of the MS-AHSS were similar to their corresponding tensile values in air. Only MS1500 charged at -1700 $mV_{Hg/HgO}$ (-1602 mV_{SHE}) had some reduction of about 100 MPa in both σ_y and σ_F. The values of the elastic modulus, evaluated from the slope of the stress-strain curve for MS1500 in air, and at -1100 $mV_{Hg/HgO}$, and -1400 $mV_{Hg/HgO}$ were quite similar; the average was about 213 GPa, close to the expected value. In contrast, the elastic modulus for MS1500 at -1700 $mV_{Hg/HgO}$ was about 185 GPa, about a 10% decrease.

As the charging potential became increasingly negative, the ductility decreased and the I values consequently increased. In the 0.1 M NaOH at -1100 $mV_{Hg/HgO}$, (-1002 mV_{SHE}), all the MS-AHSS showed no significant reduction in ductility, as reflected by the low I

values. At the higher charging potentials of -1400 and -1700 $mV_{Hg/HgO}$ (-1302 and -1602 mV_{SHE}), the four MS-AHSS exhibited significant decreased ductility and increased *I* values. From *I* of less than 10 at -1100 $mV_{Hg/HgO}$ (-1002 mV_{SHE}), the *I* increased by more than 6 times at -1400 $mV_{Hg/HgO}$ (-1302 mV_{SHE}). Except for MS1180, there were only marginal differences between the *I* values of the MS-AHSS at -1400 $mV_{Hg/HgO}$ (-1302 mV_{SHE}) and at -1700 $mV_{Hg/HgO}$ (-1602 mV_{SHE}). For instance, MS1500 charged at -1400 $mV_{Hg/HgO}$ (-1302 mV_{SHE}) had an *I* of 51; whilst at -1700 $mV_{Hg/HgO}$ (-1602 mV_{SHE}), *I* was 52. Similarly at -1400 $mV_{Hg/HgO}$ (-1302 mV_{SHE}), *I* for MS1180, MS1300 and MS1500 at -1700 $mV_{Hg/HgO}$ (-1602 mV_{SHE}) were 49, 50 and 52, respectively. In fact, all the four steels had similar I values at each charging potential.

In the 3.5wt% NaCl at E_{Zn}, the σ_{TH}, σ_F and R_A of the four MS-AHSS were similar to their values in air, and consequently all the *I* values were equal to zero.

3.4.2. Fracture characteristics in tensile tests

Similar to previous observations, the ductile and brittle behaviour of the MS-AHSS subjected to the tensile test were characterized by cup-cone and shear fracture, respectively. Table 5 indicates that a majority of the steels showed ductile cup-cone fracture, such as the steels tested in (i) air; (ii) -1100 $mV_{Hg/HgO}$ (-1002 mV_{SHE}) and -1400 $mV_{Hg/HgO}$ (-1302 mV_{SHE}) in 0.1 M NaOH; and (iii) E_{Zn} in 3.5wt% NaCl. Fig. 12 presents representative images of these cup-cone fractures viewed from the transverse side. Except in the three steels charged at -1400 $mV_{Hg/HgO}$ (-1302 mV_{SHE}), the cup-cone fractures possessed the usual characteristic morphologies. Also, all the steels charged at -1100 $mV_{Hg/HgO}$ (-1002 mV_{SHE}) had surface cracks in the neck region. The population of these cracks increased with the strength of the steel.

All the steels charged at -1700 $mV_{Hg/HgO}$ (-1602 mV_{SHE}) and the MS1500 charged at -1400 $mV_{Hg/HgO}$ (-1302 mV_{SHE}) in 0.1 M NaOH exhibited shear fractures. Fig. 13 presents typical examples of these shear fractures from the transverse side. All the shear fractures were typical, similar in features to what was previously described in 3.1.2. Also, the shear fractures were accompanied by different amounts of necking depending on the strength of the MS-AHSS. The amount of necking decreased as the strength of the steel increased.

The fracture features for MS980, MS1180 and MS1300 charged at -1400 $mV_{Hg/HgO}$ (-1302 mV_{SHE}) had a slightly different morphology than the typical cup-cone morphology. Fig. 14 shows the fractures for MS1180 and MS1300 viewed from the transverse side. While the typical cup-cone bears a flat profile when viewed from the transverse side, these steels had an

angled fracture profile, indicative of shear fracture. Fig. 15a shows the fracture in the hydrogen charged MS1180 viewed normal to the fracture surface, whilst Fig. 15b shows details of the fracture of MS1180 tested in air.

When viewed normal to the fracture surface, the features were typical of cup-cone fracture; i.e. (i) middle section consisting of microvoid coalescence (MVC) dimples and (ii) shear lip region containing elliptical MVC dimples. Closer inspection at higher magnification indicated that the middle section of the fractured steels was different from the typical cup-cone fracture. Fig. 15c-d shows details of the central region in the hydrogen-charged MS1180 and Fig. 15e shows the same details for the MS1180 tested in air. Comparing these images, the MVC dimples in the hydrogen-charged MS1180 were (i) slightly smaller and shallower and were (ii) interspersed with regions of brittle features similar to fisheyes.

4. Discussion

4.1. Cathodic charging in 3.5wt% NaCl

The values of σ_{TH} and σ_F for the four MS-AHSS measured using LISTs in air were in good agreement with the corresponding values measured using conventional tensile tests by the steel supplier. The marginal differences between the results are attributed to inter-specimen variability. This indicates that the LIST apparatus is calibrated to give accurate measurement of the yield and ultimate tensile strength.

Except for MS1500, the MS-AHSS showed minimal HE susceptibility after LIST at E_{Zn} in 3.5wt% NaCl at the lowest stress rate (~3 rph motor). MS1500 had an I of 41, while the I of the other steels ranged from 7 to 12. These results are attributed to the low hydrogen concentration in the steels for this charging condition, as indicated by the permeation test results in Table 3. The results for MS1500 were surprising given the relatively low hydrogen concentration in the MS1500 after charging at E_{Zn}. Our previous study showed no to little HE susceptibility in the four MS-AHSS at similar test conditions, with I values ranging from 0 to 10 [27]. These tests were done using a platinum electrode. In the previous study, we also did a LIST on MS1500 charged at E_{Zn} at the lowest stress rate using a graphite electrode, and measured an I of 47. This test was repeated in the current study, and MS1500 registered a slightly lower I of 41. Clearly, this difference in result may be attributed to the use of platinum counter electrode in the previous test. At sufficiently high cathodic potentials, the use of platinum counter electrode was found to reduce the hydrogen uptake of the steel

during electrochemical charging as some platinum was electroplated onto the steel surface [27]. Graphite electrodes did not exhibit this inhibiting effect on hydrogen uptake.

Table 2 indicated that the HE susceptibility of MS1300 and MS1500 increased when (i) charged at the more cathodic potential -1050 $mV_{Ag/AgCl}$ (-852 mV_{SHE}) or when (ii) tested at the lower stress rate, consistent with previous results in 0.1M NaOH [25]. The hydrogen fugacity, and the subsequent hydrogen uptake of the steel, is expected to increase with increasingly negative charging potentials. Consequently, the hydrogen sensitivity of the steel increased [51]. Low applied stress rates favour HE since hydrogen is given ample time to diffuse to critical sites (e.g. defects) and induce embrittlement [71], although it is emphasised that the hydrogen concentration was uniform throughout the specimen volume as shown by our previous modelling of the hydrogen distribution in these steels [27]. However, even though, the hydrogen global concentration was uniform, the deformation creates micro regions (i.e. crack tip) where H must locally diffuse in order to sustain sub-critical crack growth, if that is the mechanism of hydrogen embrittlement. This local diffusion process takes time and may be favoured by low applied stress rates. The fact that the H concentration is uniform does not mean that HE would take place at any applied stress rate.

Past studies have reported that HE susceptibility of AHSS correlates with hydrogen concentration, whilst hydrogen concentration correlates with strength [33]. However, the permeation test results from the current study indicate that the hydrogen concentration, measured by C_H, did not correlate with the strength. MS1300 had a somewhat higher hydrogen concentration than MS1500. This result is consistent with our previous work [27], wherein MS1300 showed a higher hydrogen concentration than MS1500 during cathodic charging in 0.1 M NaOH.

In the 3.5wt% NaCl solution, the measured D_{eff} for MS1300 and MS1500 was 12.3 x 10^{-7} cm^2 s^{-1} and 13.2 x 10^{-7} cm^2 s^{-1}, respectively. These values were in good agreement with the measured D_{eff} values in the same steels (i.e. 11.3 x 10^{-7} cm^2 s^{-1} for MS1300 and 10.2 x 10^{-7} cm^2 s^{-1} for MS1500) charged in 0.1 M NaOH, as reported in our previous work [27] and are within the known scatterband of D_{eff} values for martensitic steels [72]; i.e 1 x 10^{-7} to 1 x 10^{-5} cm^2 s^{-1} at room temperature.

The highest hydrogen concentrations in MS-AHSS were measured after cathodic charging at -1050 $mV_{Ag/AgCl}$ (-852 mV_{SHE}) in 3.5wt% NaCl; i.e. 0.137 µg g^{-1} in MS1300 and 0.115 µg g^{-1} in MS1500. Conder et al. [73] tested hydrogen concentrations in low carbon

martensite sheets (LCMS) cathodically charged in 3.5wt% NaCl solution. LCMS are steels similar to MS-AHSS in terms of carbon content and microstructure. They measured hydrogen concentrations of 0.2 μg g^{-1} and 1.3 μg g^{-1} at -900 mV_{SCE} (-654 mV_{SHE}) and -1300 mV_{SCE} (-1054 mV_{SHE}) respectively. These values are significantly higher than those in the current study, despite being in the same cathodic charging potential range. Furthermore, Conder et al did not observe any HE susceptibility in the LCMS (σ_f =1400 MPa) at these charging conditions, in contrast to the considerable HE susceptibility in MS1500 at E_{Zn} (-752 mV_{SHE}) and at -1050 $mV_{Ag/AgCl}$ (-852 mV_{SHE}). This disparity in results may be due to differences in alloy composition or microstructure, as the MS-AHSS used in the present study contained some ferrite.

Hydrogen had no influence on both σ_{TH} and σ_f but decreased the ductility of the MS-AHSS after charging at E_{Zn} or -1050 $mV_{Ag/AgCl}$ (-852 mV_{SHE}) in 3.5wt% NaCl. There were similar observations in MS-AHSS after LIST in 0.1 M NaOH at different cathodic potentials in our prior study [25].

The occurrence of cup-cone and shear fracture in hydrogen-influenced MS-AHSS has been previously observed [25, 27] and the fracture mechanism of MS-AHSS in both modes has been discussed [25]. Nevertheless, it is worthwhile to summarize these mechanisms here. In the cup-cone fracture, the central region is the fracture nucleation region. Fracture nucleation occurs by the formation and coalescence of micro-voids. As the fracture propagates, the load-bearing area decreases. As the growing fracture approaches the surface, shear stresses cause the final fracture and the shear lip region is formed. All these fracture events occur in the necked region, when the specimen is mechanically unstable in a stress-controlled test, like the LIST. These fracture events occur rapidly during the final fracture of the LIST specimen.

In contrast, in the shear fracture, fracture nucleation starts at the specimen surface, usually at a corner. The fracture extends diagonally at an angle of 45^o with respect to the direction of the tensile load, creating the characteristic angled fracture profile. As the fracture nears the other side of the specimen, the stress is amplified in the remaining load-bearing area and exceeds the fracture strength. Consequently, final fracture occurs. Again, the existence of necking indicates that these fracture events all occur during final specimen fracture, and occur quickly.

In some of the hydrogen-charged specimens, surface cracks were present in the neck region, but there were never any cracks in the uniformly deforming part of the specimen. This

indicates that hydrogen influence only manifested during the final stage of fracture when the neck was formed, and the specimen was mechanically unstable and undergoing final fracture. This observation may also suggest that stress alone may not be sufficient but that dynamic strain (deformation) is a more important (and even necessary) factor for the hydrogen embrittlement.

4.2 Influence of pH

Table 4 indicates that, as the pH of the 3.5wt% NaCl solution decreased, the HE susceptibility of MS1500 increased, as indicated by the corresponding increase in *I* values. The steel immersed in the pH 1 NaCl solution experienced the highest degree of embrittlement with *I* of 84.

The results of the test in acidified 3.5wt% NaCl gave two conclusions. Firstly, an acidic environment enhances the HE susceptibility of MS1500 in a NaCl solution. This correlates well with the predicted reduction of the hydrogen potential as pH decreases [64], and is consistent with the observation that copious amounts of hydrogen bubbles were immediately formed on the specimen upon immersion. On the other hand, the alkaline NaCl solution was actually benign to the steel. In fact, it is known that beyond pH 10, carbon steels form a passive layer than protects the steel from general corrosion [53]. Secondly, the presence of NaCl in acidic solutions significantly enhances the HE susceptibility of MS1500, as indicated by (i) the high *I*, (ii) the sharp shear fracture, and the (iii) fine and shallow MVC shear dimples in MS1500-S-pH1.

These results indicate that the combination of NaCl and low pH (i.e. < pH 3) leads to embrittlement of MS1500, and needs to be avoided in service. Pit and crevice corrosion, especially those in marine environment, could be a concern for the steel.

The MS1500 immersed in the pH 1 HCl solutions exhibited significant reduction in both σ_{TH} and σ_f. The hydrogen-induced solid solution softening has been explained as due to the interaction of hydrogen with lattice dislocations [74, 75].

The hydrogen influence on the fracture characteristic of MS1500 in the acidified 3.5wt% NaCl was manifest in the transition from cup-cone to shear fracture. Except for MS1500-S-pH3, the cup-cone and shear fractures in the steels were typical and followed the same mechanisms as described in section 3.1.2.

The fracture feature for MS1500-S-pH3 possessed a combination of cup-cone and shear fracture. The cup-cone mode dominated this fracture, as confirmed by the high R_A and

low *I*. Fracture nucleated at the centre via void coalescence that was typical of cup-cone fracture. However, the area of the central region was smaller than the typical area for steels not influenced by hydrogen. Most of the influence of hydrogen was manifest in the shear lip region. The shear lip area was blocky and coarse, which contrasted with the smooth areas for typical cup-cone failures. There were also surface shear cracks. This was the first time that such morphologies occurred in a ductile cup-cone fracture of MS1500. The most common manifestation of hydrogen influence on ductile fracture was the occurrence of surface cracks in the neck region.

The influence of hydrogen on fracture may occur preferentially near the surface, because surface cracks are twice as effective as internal cracks at causing fracture because the stress intensity factor for a surface crack is twice that of an internal crack of the same geometry [76]. Consequently, most of the brittle shear fractures in MS-AHSS were initiated at the surface. The fracture in MS1500-S-pH3 revealed a case where the hydrogen influence was not sufficient to initiate fracture nucleation at the surface. This could have occurred either due to (i) inadequate hydrogen concentration or (ii) insufficient stress. After fracture initiation and growth had occurred in the central region, some conditions appeared that favoured HE. The stress in the remaining load-bearing area increased significantly. Hydrogen is also known to be released during plastic deformation and fracture [77]. It is thus possible that some of the hydrogen in the fractured central region was released in the adjacent areas, thereby increasing the hydrogen concentration in these regions. These conditions may have collectively contributed to the embrittlement that occurred in the shear lip region.

4.3 EHE of MS1500

HE of steels is known to be favoured at low applied stress or strain rates, and even static stress conditions [54]. It is therefore expected that lower HE susceptibilities are measured in the conventional tensile test compared to other mechanical tests with slower strain or stress rates such as the SSRT or the LIST. This would explain some of the results obtained in the tensile test. For example, the MS-AHSS charged at E_{Zn} in 3.5wt% NaCl showed some HE susceptibility in the LIST; but showed no hydrogen influence, as indicated by zero *I* values, in the tensile test.

Table 5 indicated that HE susceptibility of MS-AHSS, at substantial stress rates with simultaneous hydrogen charging in 0.1 NaOH, (i) increased with increasingly negative charging potentials and (ii) and increased somewhat with increasing strength. This is consistent with our previous tests on the four MS-AHSS using the LIST with similar charging

conditions [25]. However, the measured HE susceptibilities of the steels in the previous LIST study, particularly for MS1180, MS1300 and MS1500 at the lowest stress rate in LISTs, were somewhat higher than those measured in the current work. This difference in results of the two tests could be attributed to the influence of stress rate on HE susceptibility. As earlier mentioned, substantial stress rates can produce lower sensitivity to hydrogen, as hydrogen does not have time to diffuse and accumulate to the necessary levels to cause embrittlement [71].

Table 5 shows that, in the current study, all four steel showed significant HE susceptibility at substantial stress rates with simultaneous hydrogen charging in 0.1 NaOH when charged at -1400 $mV_{Hg/HgO}$ (-1302 mV_{SHE}) and at -1700 $mV_{Hg/HgO}$ (-1602 mV_{SHE}), and there was marginal difference in the HE susceptibility of these four steels under these hydrogen charging conditions. Furthermore, there were minimal differences in the HE susceptibility of MS980, MS1300 and MS1500. These results suggest that HE susceptibility at substantial stress rates reaches a maximum or a plateau beyond a (i) critical strength and (ii) critical hydrogen concentration.

Our previous study found no HE susceptibility in the MS-AHSS tested under IHE conditions [27] at the substantial stressing rates as used in this present study. Our previous study used the same hydrogen charging as used in the current study (i.e. hydrogen charging at -1100, -1400, and -1700 $mV_{Hg/HgO}$ in 0.1 M NaOH), but hydrogen charging was conducted separately in the LIST apparatus, and then the specimen was transferred to the UTM for the subsequent mechanical testing. Our modelling of hydrogen egress indicated that 90% of the hydrogen remained in the specimen. Nevertheless, as the hydrogen charging was the only difference between the previous tests and the current tests, the lack of HE susceptibility in the previous tests is attributed in part to the small amount of egress of diffusible hydrogen from the hydrogen-charged steel during the transfer from LIST to UTM in the previous tests. It is also possible that the rate of release of hydrogen increased during the mechanical testing [77], which further reduced the hydrogen concentration in the prior tests.

In the current work, hydrogen charging was done in-situ, and the hydrogen charging was maintained even during mechanical testing. This kind of test evaluates EHE. Thus, the observed HE susceptibility in MS-AHSS in the current study was likely due to the presence of considerable hydrogen fugacity during the mechanical tests. In addition, in-situ charging is expected to maintain a constant hydrogen concentration throughout the specimen, whereas the hydrogen concentration in the pre-charged specimens was expected to be zero at the specimen surface, to increase rapidly in a diffusion profile towards the specimen centre, and

be essentially unchanged in the specimen centre, the same as during the hydrogen pre-charging. The higher hydrogen susceptibility under in-situ charging conditions can therefore be attributed to the low hydrogen concentrations at the surface for pre-charged specimens. In contrast, for in-situ hydrogen charging, the substantial hydrogen concentrations at the surface enabled hydrogen fracture events to be initiated at the specimen surface. These results leads to the conclusion that the EHE of MS-AHSS can occur more easily and at a lower equivalent fugacity than IHE, consistent with previous studies on conventional steels [68]. For IHE to occur, the existing hydrogen concentration should be high enough to accommodate for hydrogen loss during the mechanical test, particularly at the specimen surface.

It is also worth stressing that these results indicate that the HE susceptibility of a hydrogen charged specimen is lost quickly under IHE conditions, within 10 min, due to the lowering of the hydrogen concentration in the surface. The hydrogen embrittlement susceptibility can be lost without the requirement for a low hydrogen concentration throughout the specimen; it is only necessary for there to be a low surface hydrogen concentration.

Only MS1500 tested at -1700 $mV_{Hg/HgO}$ (-1602 mV_{SHE}) in 0.1 M NaOH exhibited a reduction in σ_{TH} and σ_f, in the present tests under EHE conditions The stress-strain curve presented in Fig. 11 indicated a decrease in the elastic modulus, *E*, of the steel; indicated by the reduction in the slope of the elastic region. The values of the elastic modulus, evaluated from the slope of the stress-strain curve for MS1500 in air, and at -1100 $mV_{Hg/HgO}$, and -1400 $mV_{Hg/HgO}$ were quite similar; the average was about 213 GPa, close to the expected value. In contrast, the elastic modulus for MS1500 at -1700 $mV_{Hg/HgO}$ was about 185 GPa, about a 10% decrease. This observed weakening of the atomic bonds is different to the solid solution softening of the MS-AHSS due to hydrogen [74, 75]. Solid solution softening is caused by hydrogen lowering the repulsive force between dislocations, making dislocation slip easier [74, 78]. In contrast, the decrease in the elastic modulus relates to the decreasing the cohesive bond strength between atoms [79-81] so that fracture becomes easier.

4.4 Fracture mechanism at substantial stress rates

Similar to observations in the other tests, the full influence of hydrogen on MS-AHSS subjected to substantial-applied stress rates was manifested in the occurrence of shear fractures.

The influence of hydrogen on the ductile, cup-cone fracture is evident in Fig. 12 and Fig. 15. Hydrogen induced the formation of surface cracks in the neck region of the steels charged in -1100 $mV_{Hg/HgO}$ (-1002 mV_{SHE}) in 0.1 M NaOH. The increase in the number of these cracks with increasing strength is consistent with increasing strength correlating with increased hydrogen sensitivity. Hydrogen also induced the formation of brittle fracture events that were manifest as fisheyes interspersed with the MVC dimples present in the central fracture initiation region.

This was our first case where hydrogen had clearly influenced the central crack initiation region in a cup-cone fracture. In our past work, fisheyes were present in the shear fracture of the two strongest MS-AHSS; namely MS1300 and MS1500, for LIST at the highest hydrogen fugacity and at the slowest stress rate [25]. These fisheyes were mostly found in the fracture propagation region, also interspersed with MVC shear dimples and surrounded by MVC dimples. One conclusion derived from those observations was that fisheye formation was favoured at slow stress rates, as slow rates allow hydrogen to diffuse into critical parts and cause embrittlement. Alternatively, fisheyes may be associated with a process similar to solid solution softening by hydrogen, which must be associated with the rearrangement of major dislocation arrangements by hydrogen to cause increased plasticity and to decrease the yield stress, which were experimentally observed to be slow processes. Similarly, fisheyes may be associated with such hydrogen caused dislocation rearrangement, although it is stressed that the actual fisheye formation was an extremely fast process that competed with the final ductile fracture process when the specimen was mechanically unstable and was actively undergoing final fracture.

In contrast, in the current study, the fisheyes were (i) also found in the softer steels (MS980, MS1180 and MS1300) and (ii) occurred at much higher stress rates. In light of these new observations, a review is needed of the mechanism of (i) hydrogen-influenced cup-cone fracture of MS-AHSS and (ii) fisheye formation at substantial stress rates. In our prior study where there were fisheyes under testing conditions of low applied stress rates, the fisheyes occurred during the fracture propagation stage of the shear fracture. These fisheye fracture events occurred in competition with the overall ductile micro-void coalescence processes. It is expected that there was a similar situation in the present study where the brittle fisheye fracture processes were occurring simultaneously with the ductile micro-void processes.

At this point, we propose a mechanism for fisheye formation during the fracture initiation stage. At the point of maximum load, since no fracture nucleation occurred at the surface due to lack of hydrogen influence, then microvoid nucleation and coalescence

initiated in the centre of the specimen. Hydrogen is also known to enhance dimple formation since it can induce localized plasticity [82]. As MVC dimples coalesce, the hydrogen released by the dimples accumulates locally and reaches a critical concentration. Consequently, brittle fracture occurs in these hydrogen-enriched zones and creating the 'fisheye' structure that was interspersed with the MVC dimples, and surrounded by MVC dimples.

It is clear that when the hydrogen concentration exceeds the critical amount in MS-AHSS, hydrogen embrittlement occurred as manifested by the typical shear fracture. In this case, the fracture often started at the surface (assumed at a stress concentrator), then propagated across the specimen to cause specimen rupture. This occurred for MS1500 charged at -1400 $mV_{Hg/HgO}$ (-1302 mV_{SHE}). However, for the same charging condition, MS980, MS1180 and MS1300 did not exhibit shear fracture, but instead, these three steels exhibited the hydrogen influenced cup-cone fracture presented in Fig 15, despite having *I* values almost the same as those of MS1500. This behaviour could be due to the difference in hydrogen sensitivity of the steels. It is known that as steels become stronger, the critical hydrogen concentration to cause HE decreases [54]. It may also be argued that the difference could be due to a difference in the hydrogen concentration of the steels. However, our past work has already proven that (i) there was no significant difference in the hydrogen concentration of the four MS-AHSS, and (ii) there was no correlation between the hydrogen concentration and the mechanical strength of the steels [27]. It could also be related to the ease with which hydrogen can initiate cracks at the ultimate tensile strength of the steel.

It needs to be considered that in our previous LIST test of MS1300 at -1400 $mV_{Hg/HgO}$ (-1302 mV_{SHE}) and at 30 rph [25], the steel exhibited almost similar HE susceptibility (*I* = 53) but with shear fracture. This was in contrast to the cup-cone fracture in the current study, and implies that the occurrence of shear fracture was also influenced by the stress rate.

5. Conclusions

1. There was minimal influence of hydrogen for MS980, MS1180 and MS1300 in the LIST in 3.5 wt% NaCl at E_{Zn}, (-950 $mV_{Ag/AgCl}$ (-752 mV_{SHE})), whereas MS1500 showed some HE susceptibility for this test condition.

2. The HE susceptibility of MS1300 and MS1500 was increased at the more negative potential of -1050 $mV_{Ag/AgCl}$ (-852 mV_{SHE}) in 3.5 wt% NaCl, and was increased at the lower applied stress rate.

3. The hydrogen concentration of MS1300 and MS1500 increased with increasingly negative applied potential in 3.5 wt% NaCl. However, there was no clear correlation between hydrogen concentration with the mechanical strength of the two steels.

4. The influence of hydrogen on MS1500 increased with decreasing pH in 3.5 wt% NaCl. At the same pH, the presence of NaCl increased HE susceptibility. The combination of NaCl and a critically low pH could cause HE in MS-AHSS.

5. At substantial stress rates and high hydrogen fugacity, considerable HE susceptibility occurred in the four MS-AHSS. MS1500 with in-situ hydrogen charging at -1700 $mV_{Hg/HgO}$ (-1602 mV_{SHE}) in 0.1 M NaOH showed significant solid solution softening by hydrogen (lowering of yield strength by 100 MPa) and a decrease of elastic modulus by 10%.

6. There was some degradation of mechanical strength (i.e. σ_{TH} and $\sigma_{\mp}$) of MS-AHSS (i) in the pH 1 solutions, and (ii) at substantial stress rates at the most negative charging potential in 0.1 M NaOH. This is attributed to solid solution softening by hydrogen.

7. Hydrogen influenced (i) the fracture initiation in the cup-cone fracture in MS1500 immersed in pH 3 3.5 wt% NaCl, and (ii) and the final fracture in the cup-cone fracture in M980, MS1180 and MS1300 charged at -1400 $mV_{Hg/HgO}$ (-1302 mV_{SHE}) at substantial stress rates. This manifested as fisheyes present in the central fracture initiation region, and the formation of coarse and jagged fractures in the shear lip region.

Acknowledgments

This research is supported by the Baosteel-Australia Joint Research & Development Centre (BAJC) Grant BA13037, with linkage to Baoshan Iron & Steel Co., Ltd. (Shanghai, China).

The authors also acknowledge the facilities, and the scientific and technical assistance, of the Australian Microscopy & Microanalysis Research Facility at the Centre for Microscopy and Microanalysis, The University of Queensland.

References

[1] WorldAutoSteel. Advanced High-Strength Steels Application Guidelines V5.0. Published May 5, 2014. . Available from http://www.worldautosteel.org. Accessed on July 7, 2014.
[2] Automotive Applications Council. AHSS 101-The Evolving Use of Advanced High-Strength Steels for Automotive Application. 2011. Available from http://www.autosteel.org. Accessed on April 20, 2014.
[3] X. Zhu, Z. Ma, L. Wang. Current Status of Advanced High Strength Steel for Auto-making and its Development in Baosteel. Available from http://www.baosteel.com. Accessed on May 21. 2014.
[4] ULSAB-AVC Consortium. ULSAB-AVC (Advanced Vehicle Concepts) Overview Report. Available from http://www.autosteel.org. Accessed on April 12, 2014.
[5] O. Bouaziz, H. Zurob, M. Huang, Driving Force and Logic of Development of Advanced High Strength Steels for Automotive Applications, Steel Research Int., 84 (2013) 937-947.
[6] ArcellorMittal. Usibor: Steels for Hot Stamping. Available from http://fce.arcelormittal.com. Accessed on April 12, 2014.
[7] R.Z. Mallen, S. Tarr, J. Dykeman. Recent Applications of High Strength Steels in North American Honda Production, Great Designs in Steel Seminar. Michigan, USA. Apr, 2008. Available from http://www.autosteel.org. Accessed on July 22, 2014.
[8] I. Han. Advanced High-Strength Steel Technologies in the 2014 Chevy Spark, General Motors, Great Designs in Steel 2014. Michigan, USA. May 2014. Available from http://www.autosteel.org. Accessed on July 24, 2017.
[9] E. Villalba, A. Atrens, Metallurgical aspects of rock bolt stress corrosion cracking, Mater. Sci. Eng. A, 491 (2008) 8-18.
[10] E. Villalba, A. Atrens, Hydrogen Embrittlement and Rock Bolt Stress Corrosion Cracking, Eng. Fail. Anal., 16 (2009) 164-175.
[11] E. Villalba, A. Atrens, SCC of commercial steels exposed to high hydrogen fugacity, Eng. Fail. Anal., 15 (2008) 617-641.
[12] E. Villalba, A. Atrens, An evaluation of steels subjected to rock bolt SCC conditions, Eng. Fail. Anal., 14 (2007) 1351-1393.
[13] E. Gamboa, A. Atrens, Material influence on the stress corrosion cracking of rock bolts, Eng. Fail. Anal, 12 (2005) 201-235.
[14] E. Gamboa, A. Atrens, Stress corrosion cracking fracture mechanisms in rock bolts, J Mater. Sci. , 38 (2003) 3813-3829.
[15] E. Gamboa, A. Atrens, Environmental influence on the stress corrosion cracking of rock bolts, Eng. Fail. Anal, 10 (2003) 521-558.
[16] S. Ramamurthy, A. Atrens, Stress corrosion cracking of high-strength steels, Corros. Rev., 31 (2013) 1-31.
[17] A. Oehlert, A. Atrens, SCC Propagation in Aermet 100, J. Mater. Sci. , 33 (1998) 775-781.
[18] A. Atrens, Z.F. Wang, ESEM observations of SCC initiation for 4340 high strength steel in distilled water, J Mater. Sci., 33 (1998) 405-415.
[19] A. Atrens, A. Oehlert, Linearly-increasing-stress testing of carbon steel in 4 N $NaNO_3$ and on Bayer liquor, J Mater. Sci., 33 (1998) 783-788.
[20] R.M. Rieck, A. Atrens, I.O. Smith, The Role of Crack Tip Strain Rate in the Stress Corrosion Cracking of High Strength Steels in Water, Met. Trans, 20A (1989) 889-895.
[21] L. Duprez, K. Verbeken, M. Verhaege, Effect of hydrogen on the mechanical properties of multiphase high strength steels, in: Effects of hydrogen on materials: Proceedings of the 2008 International Hydrogen Conference, Grand Teton National Park, WY, USA, 2009, pp. 62-69.

[22] T. Depover, O. Monbaliu, E. Wallaert, K. Verbeken, Effect of Ti, Mo and Cr based precipitates on the hydrogen trapping and embrittlement of Fe-C-X Q&T alloys, Int. J. Hydrogen Energ., 40 (2015) 16977-16984.
[23] D. Pérez Escobar, C. Miñambres, L. Duprez, K. Verbeken, M. Verhaege, Internal and surface damage of multiphase steels and pure iron after electrochemical hydrogen charging, Corros. Sci., 53 (2011) 3166-3176.
[24] Q. Liu, A. Atrens, The influence of hydrogen on the low cycle fatigue behavior of medium strength 3.5NiCrMoV steel studied using notched specimens, Adv.Eng. Mater., DOI: 10.1002/adem.201700680 (2017).
[25] J. Venezuela, Q. Liu, M. Zhang, Q. Zhou, A. Atrens, The influence of hydrogen on the mechanical and fracture properties of some martensitic advanced high strength steels studied using the linearly increasing stress test, Corros. Sci., 99 (2015) 98-117.
[26] J. Venezuela, Q. Liu, M. Zhang, Q. Zhou, A. Atrens, A review of hydrogen embrittlement of martensitic advanced high-strength steels, Corros. Rev., 34 (2016) 153-186.
[27] J. Venezuela, Q. Zhou, Q. Liu, M. Zhang, A. Atrens, Influence of hydrogen on the mechanical and fracture properties of some martensitic advanced high strength steels in simulated service conditions, Corros. Sci., 111 (2016) 602-624.
[28] Q. Liu, Q. Zhou, J. Venezuela, M. Zhang, A. Atrens, Hydrogen Concentration in Dual-Phase (DP) and Quenched and Partitioned (Q&P) Advanced High-Strength Steels (AHSS) under Simulated Service Conditions Compared with Cathodic Charging Conditions, Adv. Engg. Mater., 18 (2016) 1588-1599.
[29] Q. Liu, J. Venezuela, M. Zhang, Q. Zhou, A. Atrens, Hydrogen trapping in some advanced high strength steels, Corros. Sci., 111 (2016) 770-785.
[30] Q. Liu, Q. Zhou, J. Venezuela, M. Zhang, J.Wang, A. Atrens, A review of the influence of hydrogen on the mechanical properties of DP, TRIP, and TWIP advanced high-strength steels for auto construction, Corros. Rev., 34 (2016) 127-152.
[31] T. Depover, L. Duprez, K. Verbeken, E. Wallaert, M. Verhaege, In-situ mechanical evaluation of hydrogen embrittlement for TRIP, FB, DP and HSLA steels, in: Steely Hydrogen Conference, Ghent Belgium, 2011, pp. 31-42.
[32] T. Depover, D. Escobar, E. Wallaert, Z. Zermout, K. Verbeken, Effect of hydrogen charging on the mechanical properties of advanced high strength steels, Int. J. Hydrogen Energ., 39 (2014) 4647-4656.
[33] M. Loidl, O. Kolk, S. Veith, T. Gobel, Characterization of hydrogen embrittlement in automotive advanced high strength steels, Mat.-wiss. u.Werkstofftech, 42 (2011).
[34] G. Lovicu, M. Bottazzi, F. D'Aiuto, M. De Sanctis, A. Dimatteo, C. Santus, R. Valentini, Hydrogen embrittlement of automotive advanced high-strength steels, Metall. Mater. Trans. A., 43 (2012) 4075-4087.
[35] J.A. Ronevich, J.G. Speer, D.K. Matlock, Hydrogen embrittlement of commercially produced advanced high strength steels, SAE Int. J. Mater. Manuf., 3 (2010) 255-267.
[36] J. Venezuela, Q. Zhou, Q. Liu, M. Zhang, A. Atrens, Hydrogen trapping in some automotive martensitic advanced high-strength steels, Adv. Eng. Mater., 1700468. doi:10.1002/adem.201700468 (2017).
[37] J. Venezuela, E. Gray, C.V. Tapia-Bastidas, Q. Liu, Q. Zhou, M. Zhang, A. Atrens, Equivalent hydrogen fugacity during electrochemical charging of some martensitic advanced high-strength steels, Corros Sci, 127 (2017) 45-58.
[38] Q. Liu, E. Gray, J. Venezuela, Q. Zhou, C. Tapia-Bastidas, M. Zhang, A. Atrens, Equivalent Hydrogen Fugacity during Electrochemical Charging of 980DP Steel Determined by Thermal Desorption Spectroscopy, Advanced Engineering Materials, DOI: 10.1002/adem.201700469 (2018) (2017).

[39] Q. Liu, Q. Zhou, J. Venezuela, M. Zhang, A. Atrens, Hydrogen influence on some advanced high-strength steels, Corrosion Science, 125 (2017) 114-138.
[40] Q. Liu, A. Atrens, A critical review of the influence of hydrogen on the mechanical properties of medium strength steels, Corros. Rev., 31 (2013) 85-104.
[41] S. Ramamurthy, W.M.L. Lau, A. Atrens, Influence of the applied stress rate on the stress corrosion cracking of 4340 and 3.5NiCrMoV steels under conditions of cathodic hydrogen charging. , Corros. Sci., 53 (2011) 2419-2429.
[42] S. Ramamurthy, A. Atrens, The influence of applied stress rate on the stress corrosion cracking of 4340 and 3.5NiCrMoV steels in distilled water at 30 °C, Corros. Sci., 52 (2010) 1042-1051.
[43] J.Q. Wang, A. Atrens, D.R. Cousens, P.M. Kelly, C. Nockolds, S. Bulcock, Measurement of grain boundary composition for X52 pipeline steel, Acta Mater., 46 (1998).
[44] H. Lukito, Z. Szklarska-Smialowska, Susceptibility of medium-strength steels to hydrogen-induced cracking, Corros. Sci., 39 (1997) 2151-2169.
[45] A. Oehlert, A. Atrens, Environmental Assisted Fracture For 4340 Steel in Water and Air of Various Humidities, J Mater. Sci., 32 (1997) 6519-6523.
[46] A. Oehlert, A. Atrens, Initiation and Propagation of Stress Corrosion Cracking in AISI 4340 and 3.5NiCrMoV Rotor Steel in Constant Load Tests, Corros. Sci., 38 (1996) 1159-1170.
[47] S. Ramamurthy, A. Atrens, The Stress Corrosion Cracking of As-Quenched 4340 and 3.5NiCrMoV Steels Under Stress Rate Control in Distilled Water at 90C Corros. Sci., 34 (1993) 1385-1402.
[48] N.N. Kinaev, D.R. Cousens, A. Atrens, The Crack Tip Strain Field of AISI 4340 Part III Hydrogen Influence, J Mater. Sci. , 34 (1999) 4931-4936.
[49] M.C. Zhao, M. Liu, A. Atrens, Y.Y. Shan, K. Yang, Effect of applied stress and microstructure on sulfide stress cracking resistance of pipeline steels subject to hydrogen sulfide, Mater. Sci. Eng. A, (2008) 43-47.
[50] R.P. Gangloff, Hydrogen assisted cracking of high strength alloys, in: I. Milne, R.O. Ritchie, B. Karihaloo (Eds.) Comprehensive structural integrity Vol. 6, Environmentally Assisted Fracture, Elsevier, 2003, pp. 31 - 101.
[51] S. Lynch, Hydrogen embrittlement phenomena and mechanisms, Corros. Rev., 30 (2012) 105-123.
[52] C. Willan. Hydrogen Embrittlement A Historical Overview. Available from www.omegaresearchinc.com/. Accessed on July 25, 2017.
[53] D.A. Jones, Principles and prevention of corrosion, 2nd Ed., Prentice Hall, NJ, 1996.
[54] M. R. Louthan Jr, Hydrogen Embrittlement of Metals: A Primer for the Failure Analyst, J Fail. Anal. and Preven., 8 (2008) 289-307.
[55] A. Atrens, C.C. Brosnan, S. Ramamurthy, A. Oehlert, I.O. Smith, Linearly increasing stress test (LIST) for SCC research, Meas. Sci. Technol., 4 (1993) 1281-1292.
[56] J. Salmond, A. Atrens, SCC of copper using the linearly increasing stress test, Scripta Met. Mater., 26 (1992) 1447-1450.
[57] A. Atrens, J.Q. Wang, K. Stiller, H.O. Andren, Atom probe field ion microscope measurements of carbon segregation at an alpha:alpha grain boundary and service failures by intergranular stress corrosion cracking, Corros. Sci., 48 (2006) 79-92.
[58] N. Winzer, A. Atrens, W. Dietzel, G. Songa, K.U. Kainer, Comparison of the linearly increasing stress test and the constant extension rate test in the evaluation of transgranular stress corrosion cracking of magnesium, Mater. Sci. Eng. A, 472 (2008) 97-106.
[59] S. Ramamurthy, W.M.L Lau, A. Atrens, Influence of the applied stress rate on the stress corrosion cracking of 4340 and 3.5NiCrMoV steels under conditions of cathodic hydrogen charging, Corrosion Science, 53 (2011) 2419-2429.

[60] Q. Liu, B. Irwanto, A. Atrens, The Influence of Hydrogen on 3.5NiCrMoV steel studied using the linearly increasing stress test. , Corros. Sci., 67 (2013) 193-203.
[61] Q. Liu, B. Irwanto, A. Atrens, Influence of hydrogen on the mechanical properties of some medium-strength Ni–Cr–Mo steels, Mater. Sci. Eng. A, 617 (2014) 200-210.
[62] F. Cao, Z. Shi, G. Song, M. Liu, M. Dargusch, A. Atrens, Stress corrosion cracking of several solution heat-treated Mg–X alloys, Corros. Sci., 96 (2015) 121-132.
[63] Q. Liu, A.D. Atrens, Z. Shi, K. Verbeken, A. Atrens, Determination of the hydrogen fugacity during electrolytic charging, Corros. Sci., 87 (2014) 239-258.
[64] M. Pourbaix, Atlas of electrochemical equilibria in aqueous solutions (English edition), Pergamon press, Oxford, 1966.
[65] M. Nishimoto, J. Ogawa, I. Muto, Y. Sugawara, N. Hara, Simultaneous visualization of pH and Cl− distributions inside the crevice of stainless steel, Corrosion Science, 106 (2016) 298-302.
[66] I. M. Bernstein, R. Garber, G. M. Pressouyre, Effect of Hydrogen on Behavior of Materials, in: A.W. Thompson, I.M. Bernstein (Eds.) Effect of hydrogen on behavior of materials, TMS-AIME, New York, 1976, pp. 37.
[67] W.W. Gerberich, T. Livne, X. Chen, Modeling Environmental Effects on Crack Growth Processes, , TMS, Warrendale, PA, 1985.
[68] R.J. Walter, R.P. Jewett, W.T. Chandler, On the mechanism of hydrogen-environment embrittlement of iron- and nickel-base alloys, Mater. Sci. Eng., 5 (1970) 99-110.
[69] T. Zakroczymski, Adaptation of the electrochemical permeation technique for studying entry, transport and trapping of hydrogen in metals, Electrochim. Acta, 51 (2006) 2261-2266.
[70] Q. Liu, A. Atrens, Reversible hydrogen trapping in a 3.5NiCrMoV medium strength steel, Corros. Sci., 96 (2015) 112-120.
[71] M. Hashimoto, R.M. Latanision, The Role of Dislocations during Transport of Hydrogen in Hydrogen Embrittlement of Iron, Metall. Trans. A. , 19A (Nov 1988) 2799-2803.
[72] T. Bollinghaus, H. Hoffmeister, C. Middel, Scatterbands for hydrogen diffusion coefficients in steels having ferritic or martensitic microstructures and steels having an austenitic microstructure at room temperature, Weld World, 37 (1996) 16-23.
[73] R.J. Conder, P. Felton, R. Burke, P. Dent, Hydrogen Embrittlement Testing Of High Strength Low Carbon Martensitic Steels, Corrosion 2015, NACE International, San Antonio, Texas, in, 2010.
[74] C.D. Beachem, A new model for hydrogen assisted cracking (Hydrogen embrittlement), Metall. Trans., 3 (1972) 437 – 451.
[75] M. Nagumo, Fundamentals of Hydrogen Embrittlement, Springer, Singapore, 2016.
[76] G. Dieter, Mechanical Metallurgy, 3rd Ed., McGraw-Hill, NY, USA, 1988.
[77] H. Shoda, H. Suzuki, K. Takai, Y. Hagiwara, Hydrogen Desorption Behavior of Pure Iron and Inconel 625 during Elastic and Plastic Deformation, ISIJ Int., 50 (2010) 115-123.
[78] H.K. Birnbaum, P.Sofronis, Hydrogen-enhanced localized plasticity - a mechanism for hydrogen-related fracture, Mater. Sci. Engg. A, 176 (1994) 191-202.
[79] A.R. Troiano, The role of hydrogen and other interstitials in the mechanical behavior of metals, Trans. ASM, 52 (1960) 54 - 80.
[80] R.A. Oriani, A mechanistic theory of hydrogen embrittlement of steels, Ber. Bunsenges. Phys. Chem., (1972) 848 - 857.
[81] R. A. Oriani, P. H. Josephic, Testing of the decohesion theory of hydrogen-induced crack propagation, Scripta Metall, 6 (1972) 681-688.
[82] D.C. Ahn, P. Sofronis, R.H. Dodds, On hydrogen-induced plastic flow localization during void growth and coalescence, Int. J. Hydrogen Energ., 32 (2007) 3734-3742.

Fig. 1. Schematic of a LIST specimen. Dimensions are in mm. The specimen thicknesses were: (i) 1.5 mm for MS980, (ii) 1.70 mm for MS1180, (iii) 1.20 mm for MS1300, and (iv) 1.18 mm for MS1500

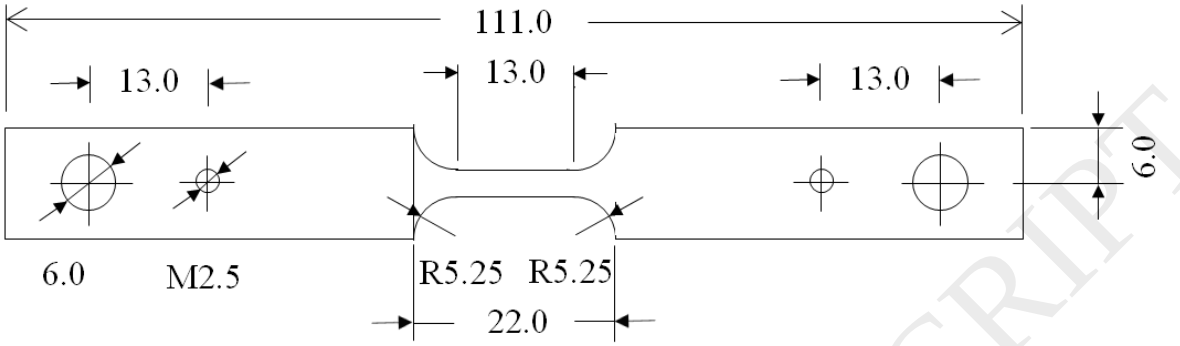

Fig. 2. Typical plots of potential drop versus stress obtained from a LIST. The threshold stress, σ_{TH}, was determined as the transition stress corresponding to the significant increase in the slope. The two plots have been displaced vertically for ease of viewing.

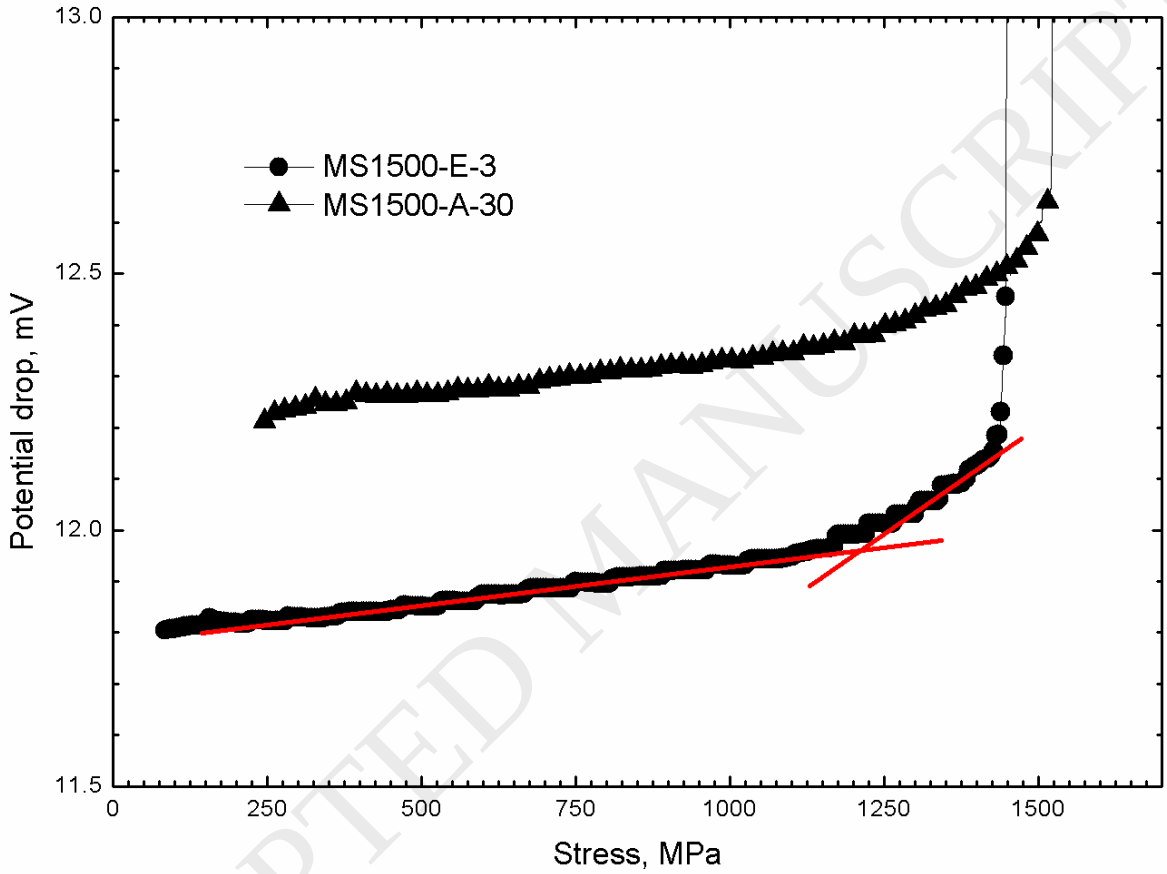

Fig. 3. (a) A typical ductile cup-cone fracture (specimen: MS1500-A-30 tested in air) and (b) a typical shear fracture (specimen: MS1500-E-3 tested in 3.5wt%NaCl). The arrow shows the direction of the applied tensile load. The mean thickness of the MS1500 specimen was 1.18 mm.

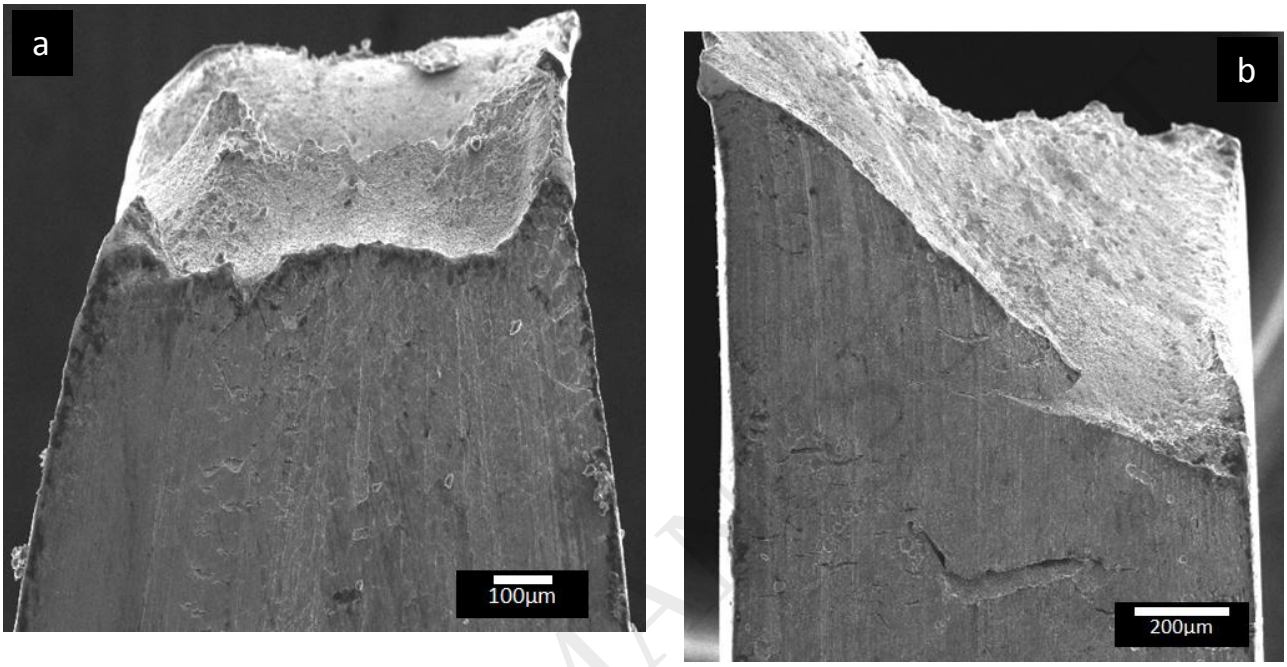

Fig. 4. (a) Normal (or top) view of a typical cup-cone fracture; the arrows show the fracture propagation directions. High magnification images show details of (b) the central (C) region and (c) shear lip (S) region consisting of round and parabolic MVC dimples, respectively. (Specimen: MS1500-A-30 tested in air).

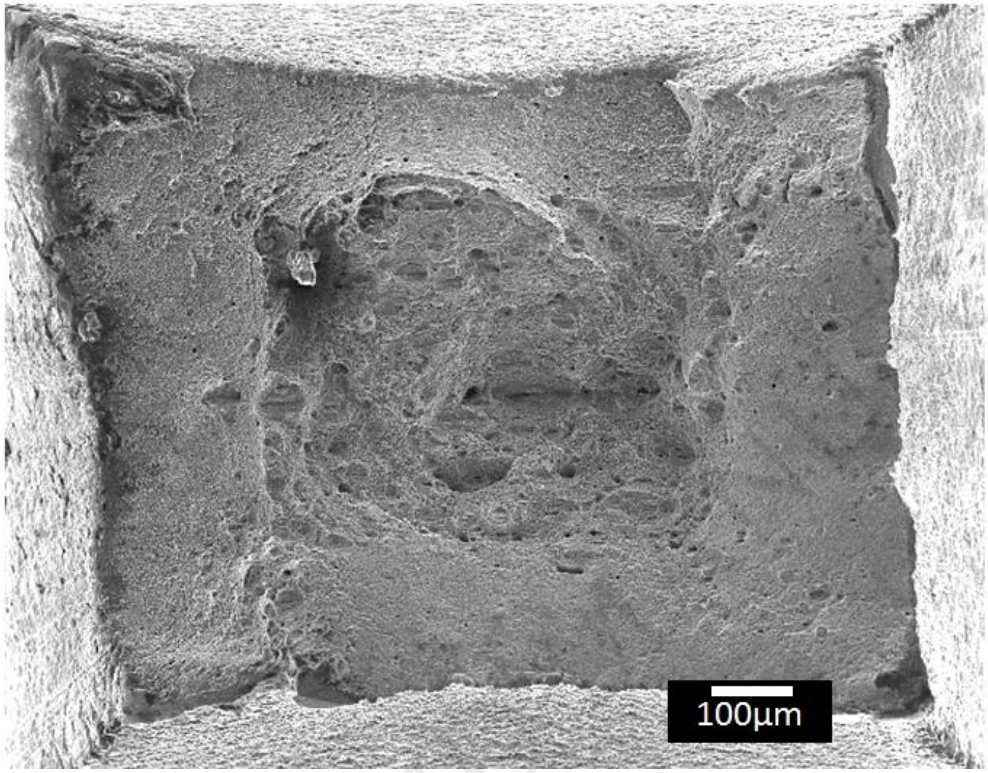

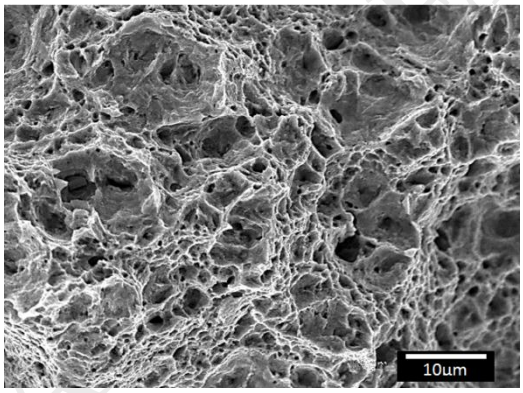

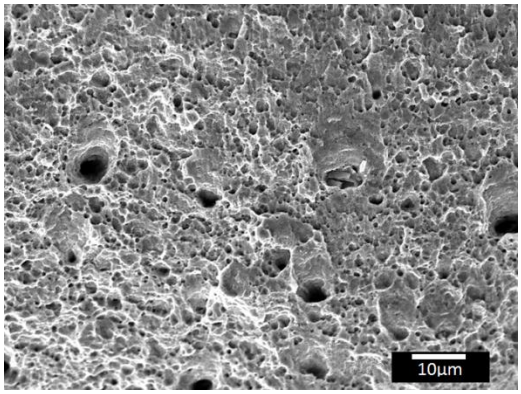

Fig. 5. (a) Normal (or top) view of a typical shear fracture. The arrows show the fracture propagation directions. High magnification images show details of (b) the fracture initiation ('I') region with a mixture of intergranular and quasi-cleavage fracture features; (c) fracture propagation ('P') region consisted of shallow shear MVC dimples; and (d) final fracture ('F') region consisting of brittle features similar to those in region "I". (specimen: MS1500-E-3 tested in 3.5wt% NaCl).

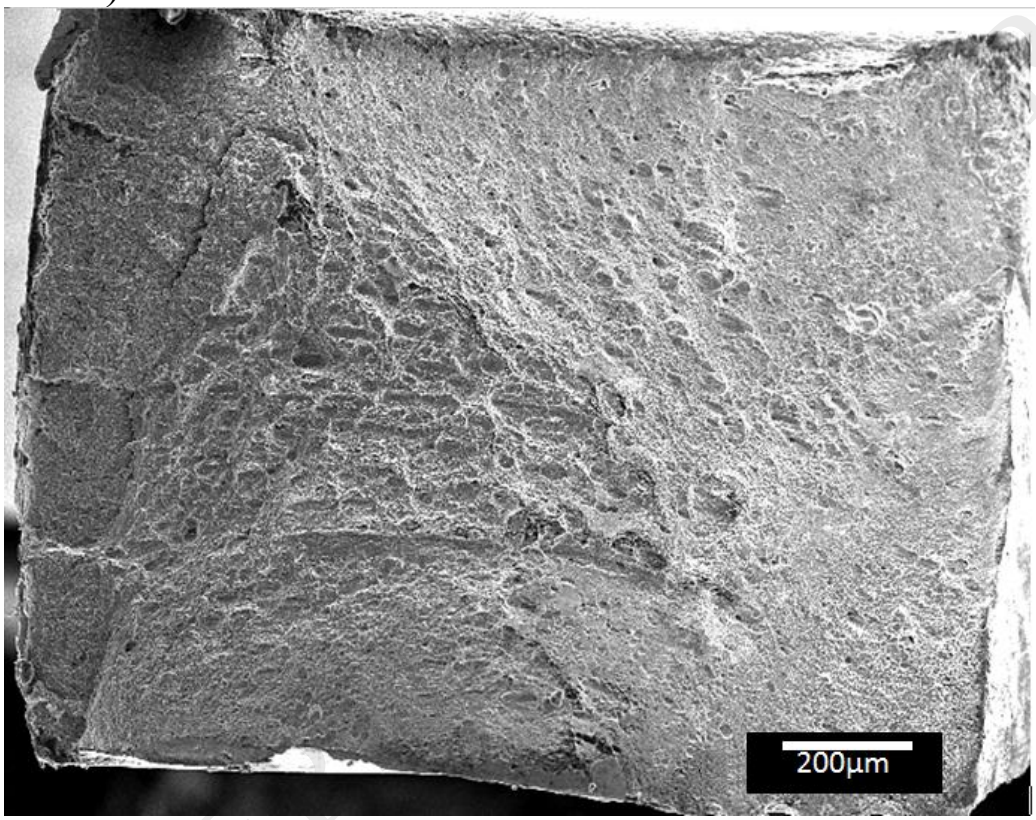

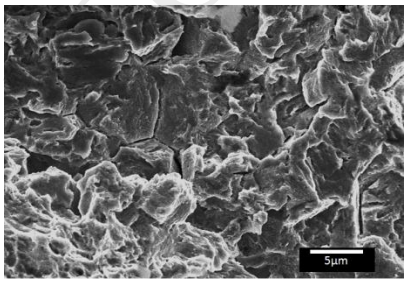

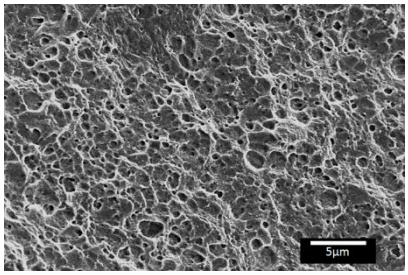

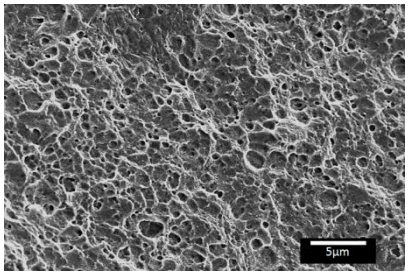

Fig. 6 (a) A typical permeation transient loop obtained from the permeation tests using MS1500 steel. The solutions in the entry cell and exit cell consisted of 3.5 wt% NaCl and 0.1 M NaOH, respectively. The permeation transients were as follows: (i) successive decay transients from -1050 to -950, then -950 to -850 $mV_{Ag/AgCl}$; and (ii) successive rise transients from -850 to -950, then -950 to -1050 $mV_{Ag/AgCl}$. The arrows indicate the time at which the new constant potential was applied to the hydrogen entry side of the permeation specimen. The permeation transient measured the current density at the exit side of the permeation specimen (which represents the flux of hydrogen, which had permeated through the specimen. (b) An experimental rise permeation transient (-850 to -950 $mV_{Ag/AgCl}$) fitted to the appropriate mathematical model.

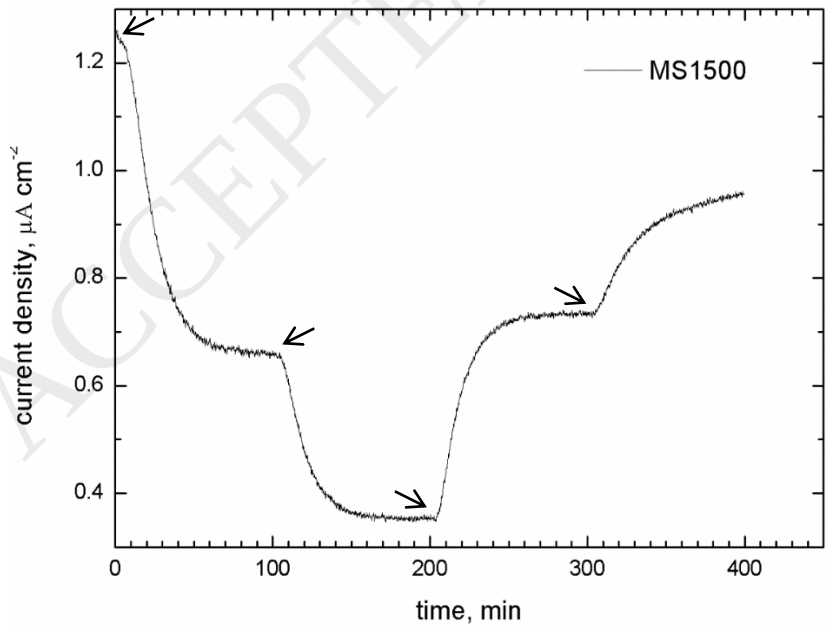

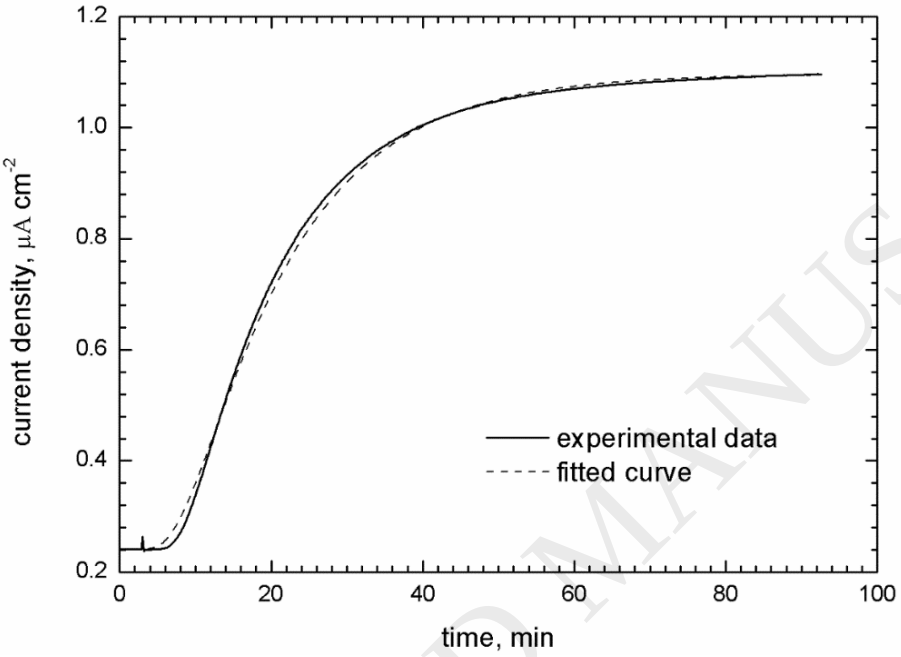

Fig. 7. Cup-cone fractures for MS1500 in the 3.5wt% NaCl solution at (a) pH 5, (b) pH 7, and (c) pH 9.

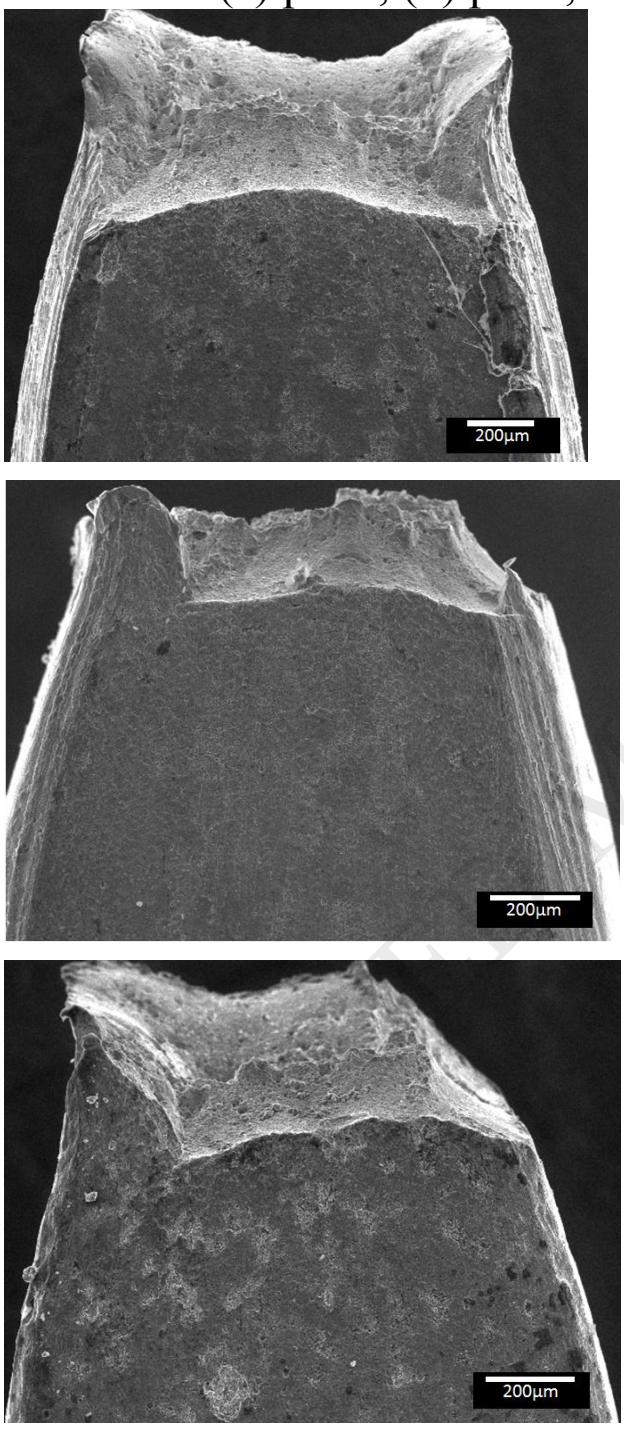

Fig. 8. Comparison of the shear fractures for MS1500 in the (a) pH 1 3.5wt% NaCl solution and in the (b) NaCl-free pH 1 HCl solution.

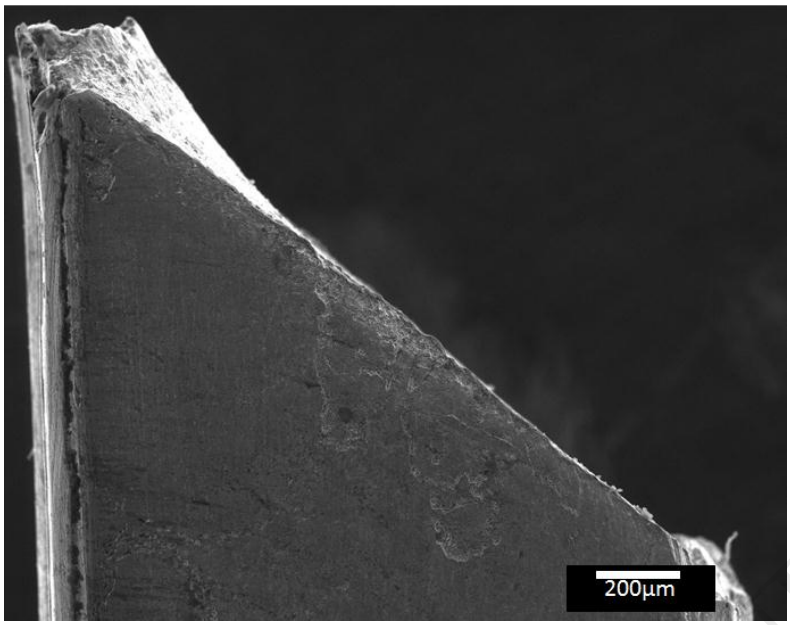

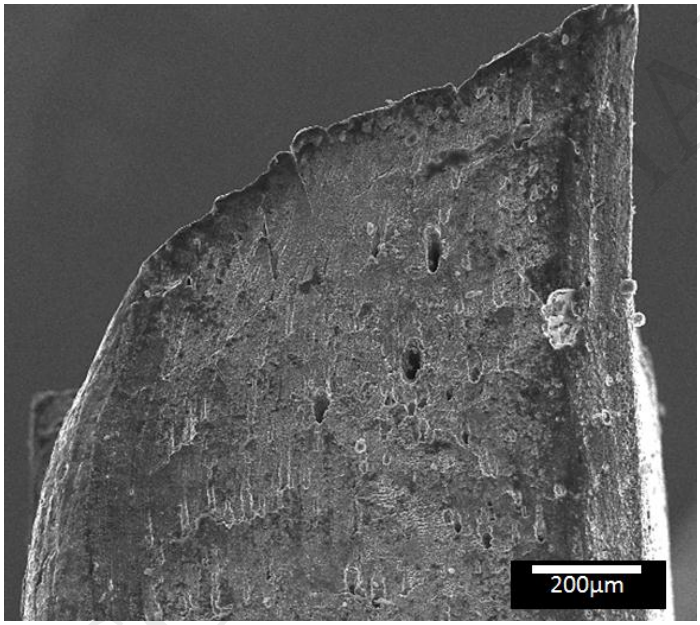

Fig. 9. Comparison of the shear fracture for MS1500 in (a) the NaCl-free pH 1 HCl solution and (b) pH 1 3.5wt% NaCl solution. Details of the 'P' region for (c) MS1500-pH1 and (d) MS1500-S-pH1. Arrow shows direction of crack propagation. .

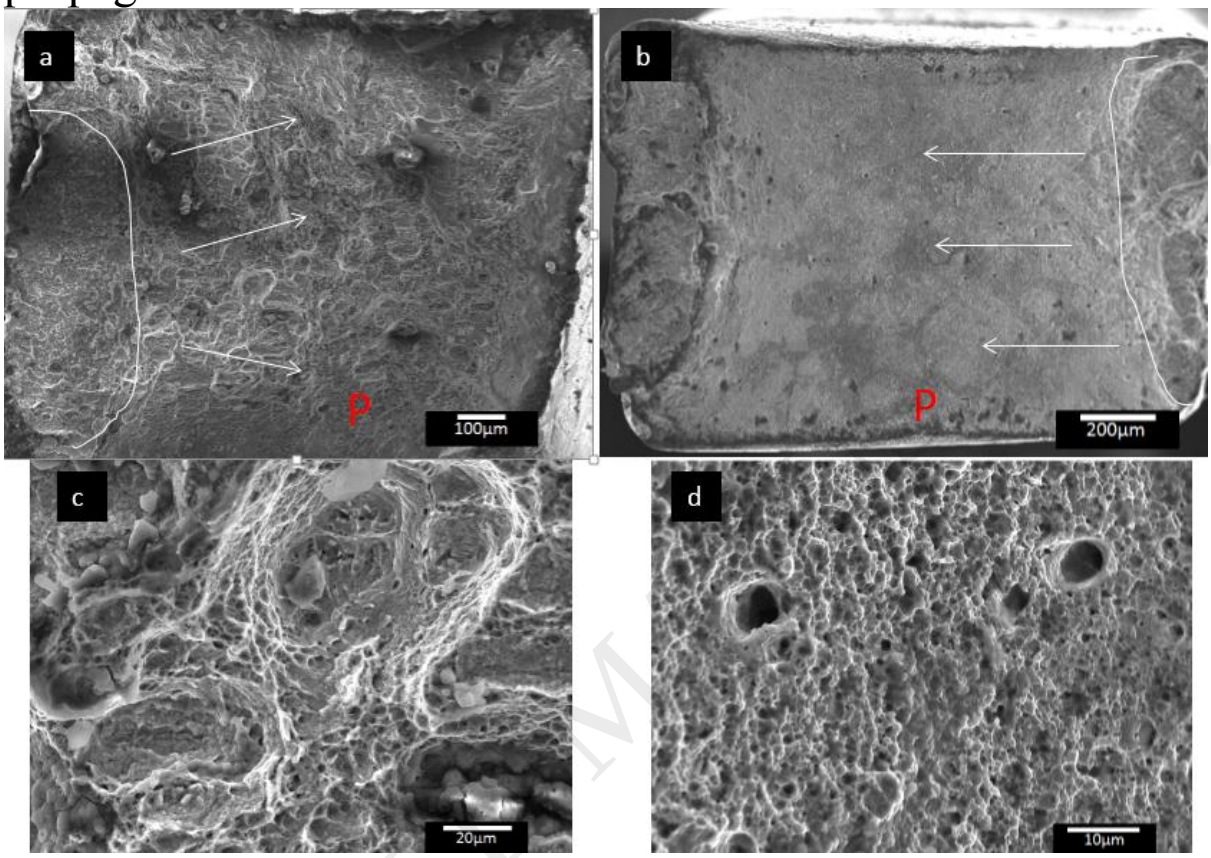

Fig. 10. Details of the fracture surface for MS1500 after LIST in pH 3 3.5 wt% NaCl solution at a stress rate of 0.08 MPa s^{-1}; viewed (a) normal to the fracture surface, and from (b) the wide transverse side and (c) the short transverse side. This fracture possessed a mix of cup-cone and shear fracture features

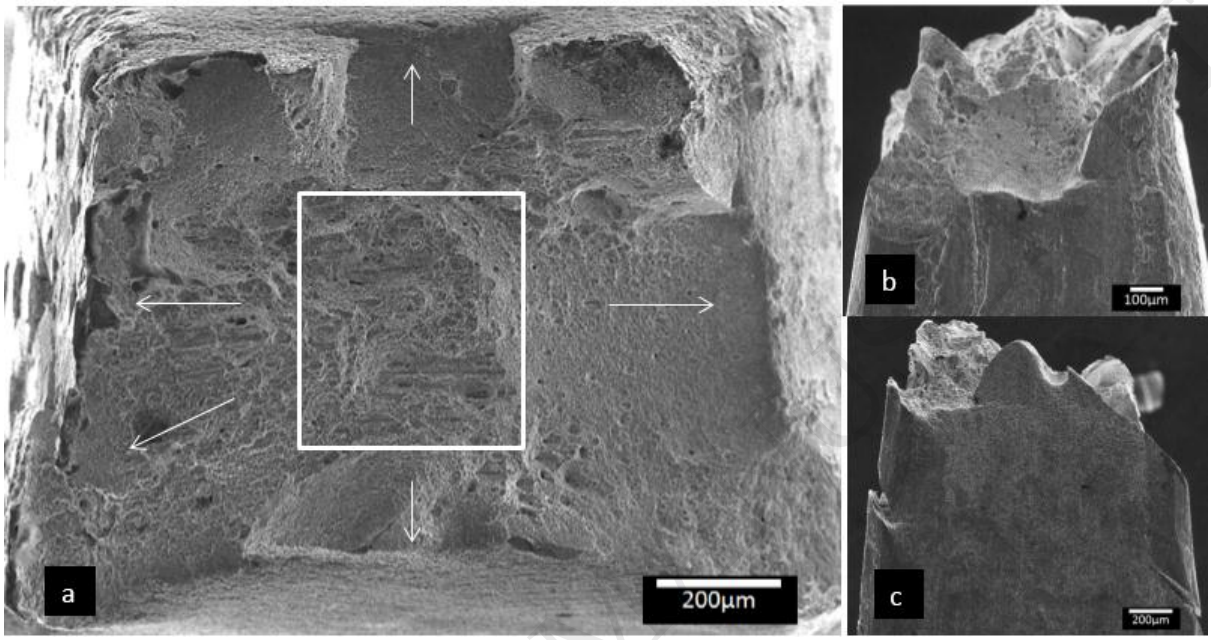

Fig. 11. Stress-strain curve for MS1500 in air, and with precharging and simultaneous in-situ hydrogen charging at -1100, -1400 and -1700 $mV_{Hg/HgO}$ in 0.1 M NaOH

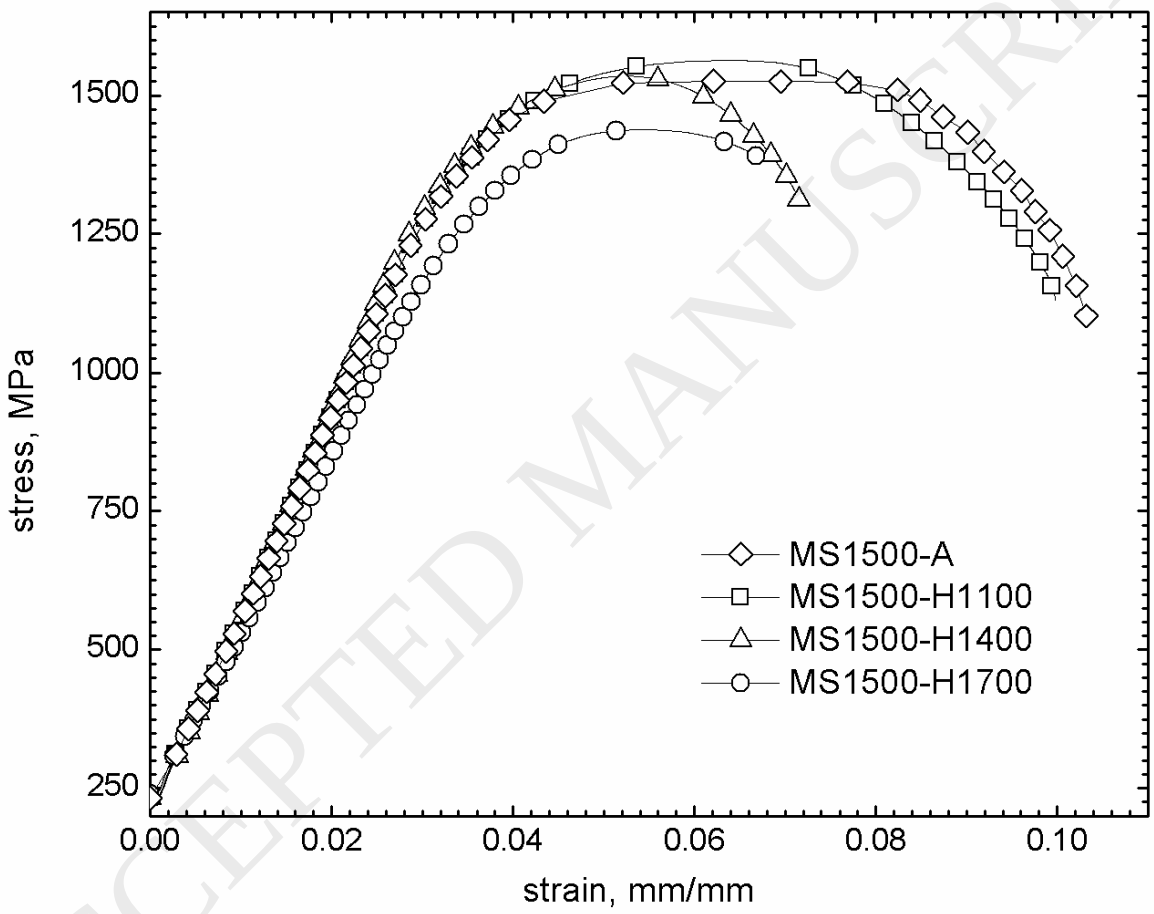

Fig. 12. Cup-cone fractures in tensile test specimens as viewed from the transverse side: (a) MS980 and (b) MS1500 charged at E_{zn} in 3.5 wt% NaCl. (c) MS980 and (d) MS1500 charged at -1100 $mV_{Hg/HgO}$ in 0.1 M NaOH; all showing surface cracks in the neck region.

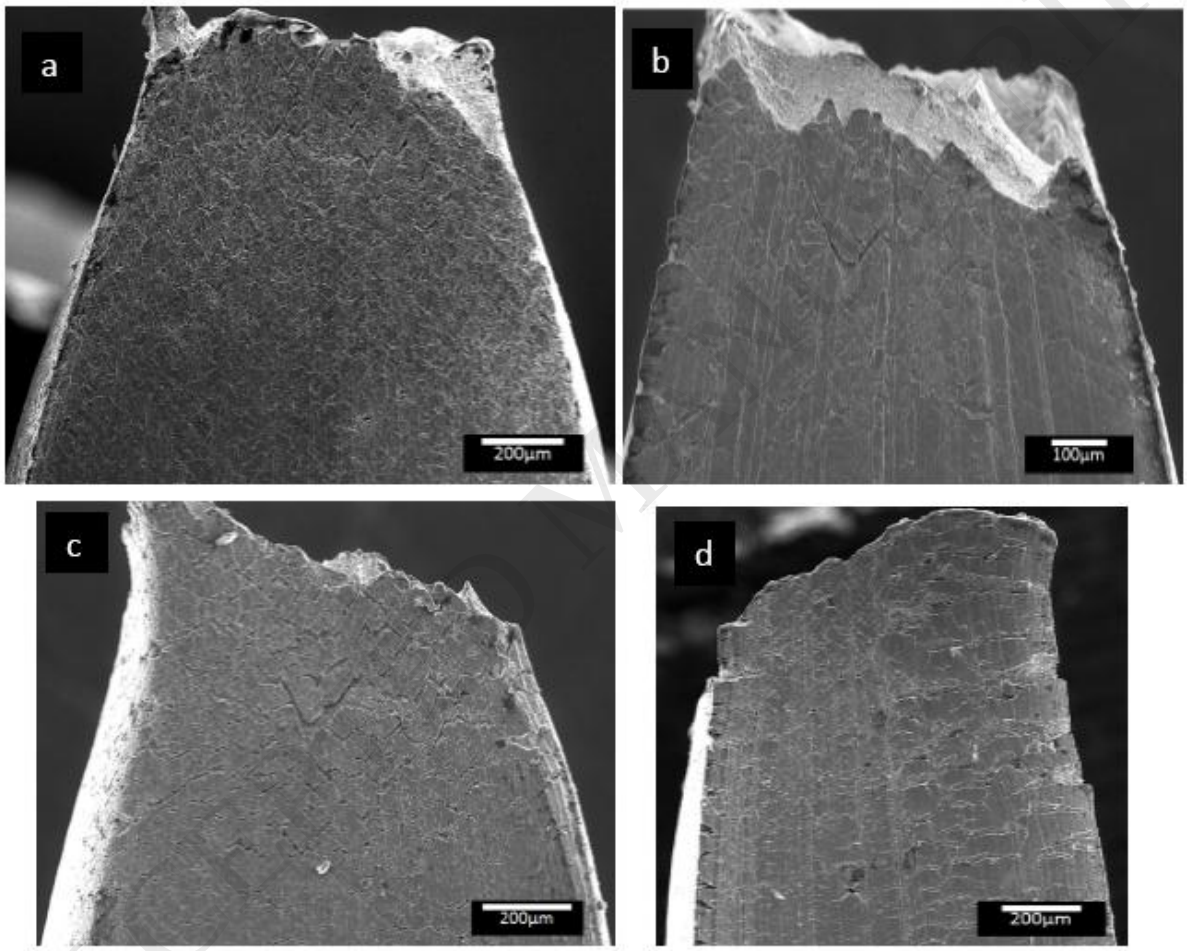

Fig. 13. Fracture images of (a) MS980, (b) MS1180, (c) MS1300 and (b) MS1500 all charged at -1700 $mV_{Hg/HgO}$ in 0.1 M NaOH. The view is from the transverse side. All the fractures were shear, but accompanied by decreasing amounts of necking with increasing strength of the MS-AHSS.

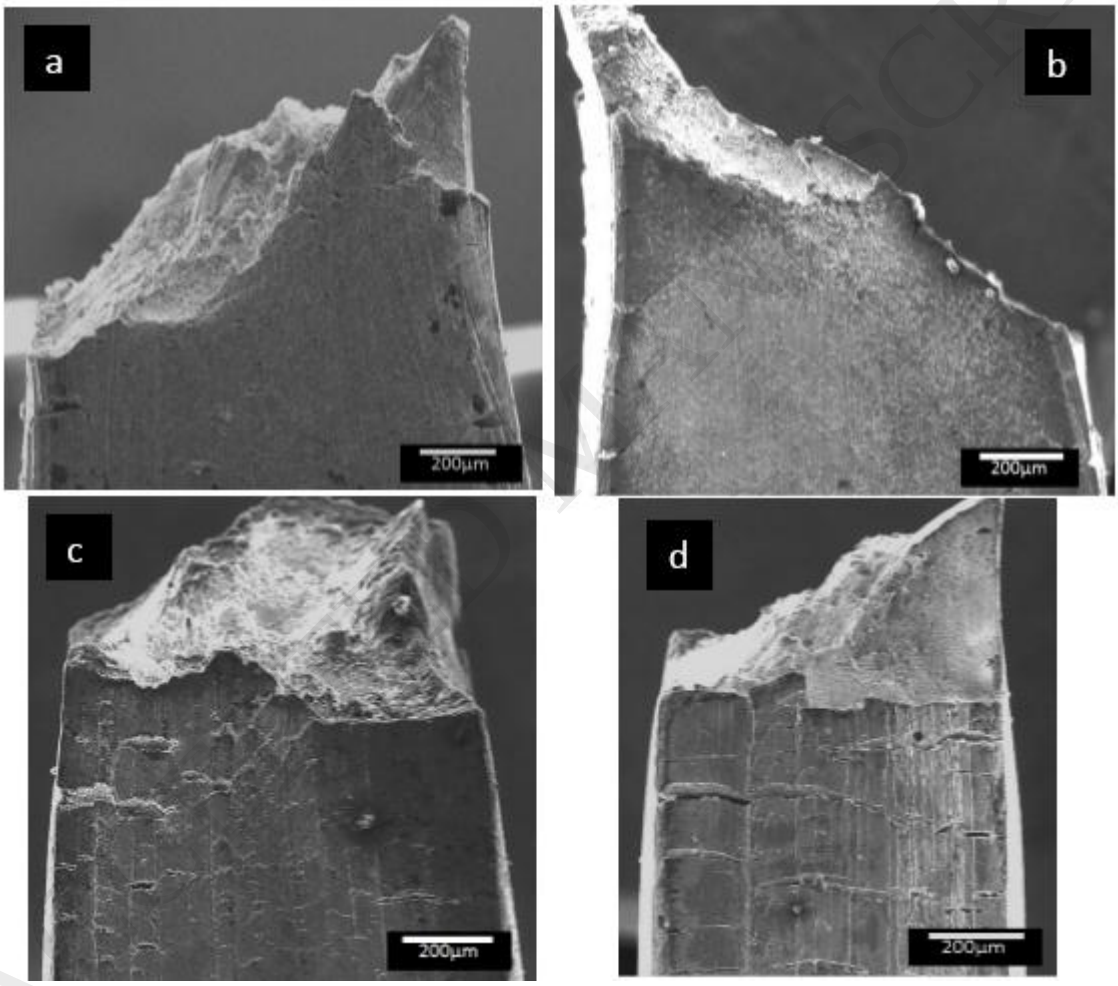

Fig. 14. Details of the fracture of (a) MS1180 and (b) MS1300 charged at -1400 $mV_{Hg/HgO}$ in 0.1 M NaOH viewed from the wide transverse side. These specimens possess a shear fracture profile but with a fracture mode that was akin to a cup-cone fracture

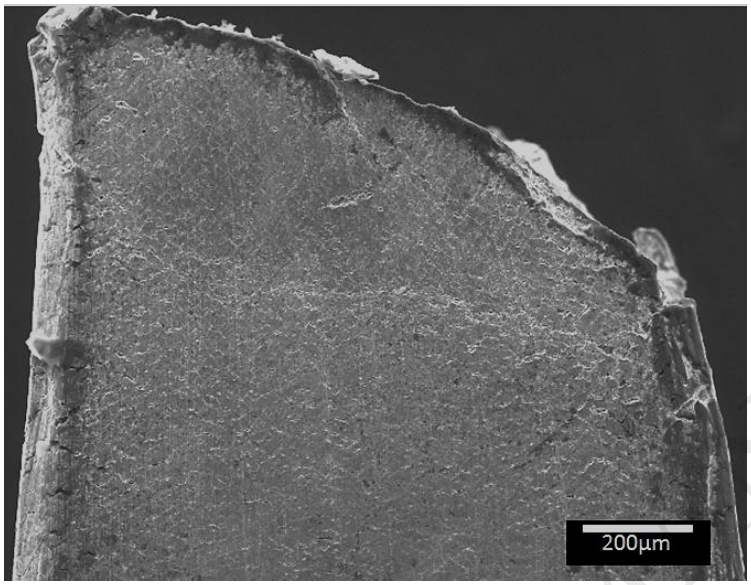

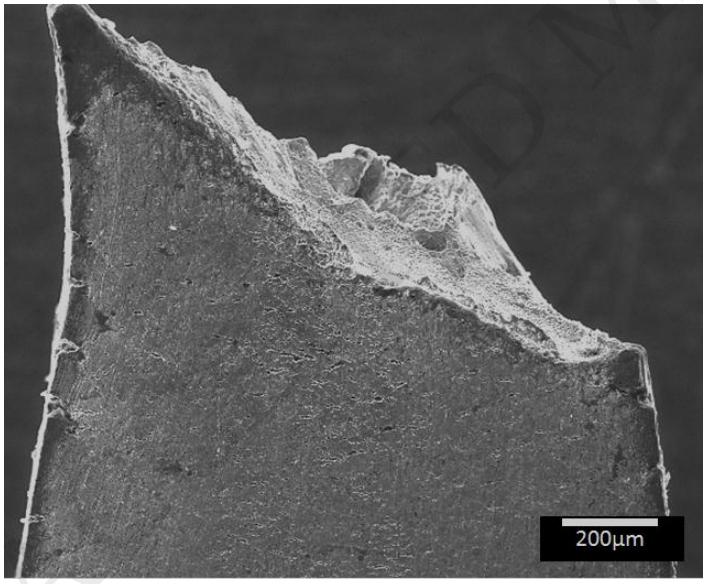

Fig. 15. Details of the fracture surface of MS1180 (a) charged at -1400 $mV_{Hg/HgO}$ in 0.1 M NaOH compared with the same steel tested in (b) air. Arrows shows crack propagation directions. Magnified images of the central region of : (c-d) hydrogen charged MS1180 consisting of a mix of MVC dimples interspersed with circular brittle regions similar to fisheyes, and (e) MS1180 in air consisting of typical MVC dimples.

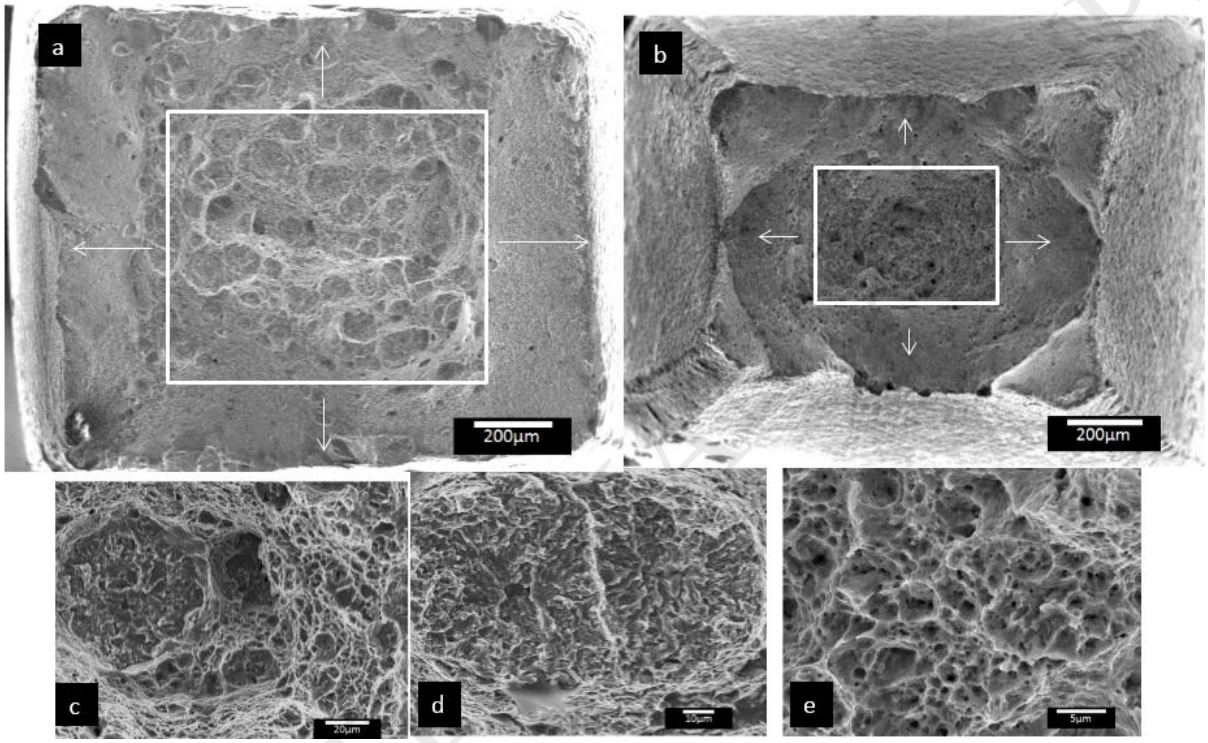

Table 1 Chemical composition (in wt %), microstructural composition (in %), and mechanical properties of the MS-AHSS.

Steel designation	C	Si	Mn	S	P	Al	Ti	Cr	% martensite	% ferrite	Yield stress, MPa	Tensile stress, MPa	e_f, %
MS980	0.12	0.37	1.63	<0.01	<0.01	0.03	0.04	0.02	70	30	883	1070	5
MS1180	0.15	0.37	1.64	<0.01	<0.01	0.03	0.03	0.02	84	16	1176	1355	3
MS1300	0.15	0.39	1.67	<0.01	<0.01	0.04	0.03	0.01	90	10	1108	1367	2.9
MS1500	0.19	0.36	1.51	<0.01	<0.01	0.04	0.03	0.02	92	8	1326	1512	2.4

Table 2 LIST results for different MS-AHSS in (a) air or in (b) 3.5wt% NaCl solution, at the two charging potentials: (i) E_{Zn} = -950 $mV_{Ag/AgCl}$ (-752 mV_{SHE}) and (ii) -1050 $mV_{Ag/AgCl}$ (-852 mV_{SHE}). The applied stress rates are given and were equivalent to those produced by the 30 (intermediate) and 3 (slow) rph motors. Unless otherwise noted in 'Remarks', fractures were ductile, accompanied by necking and cup-cone fracture, and MVC dimples present on fracture surface. n/a means not applicable.

Specimen designation	Environment	Potential, $mV_{Ag/AgCl}$	Applied stress rate, MPa s^{-1}	Threshold or yield stress, σ_{TH}, MPa (±5)	Fracture stress, UTS, σ_F, MPa (±2)	Reduction in area, R_A, %	Hydrogen embrittlement index, I	Remarks
MS980-A-30	Air	n/a	0.064	910	1040	73	n/a	
MS1180-A-30	Air	n/a	0.054	1170	1342	71	n/a	
MS1300-A-30	Air	n/a	0.080	1120	1308	65	n/a	
MS1500-A-30	Air	n/a	0.080	1310	1518	61	n/a	
MS980-Ezn-3	NaCl	-950	0.0064	900	1010	68	7	.
MS1180-Ezn-3	NaCl	-950	0.0054	1175	1310	66	7	
MS1300-Ezn-3	NaCl	-950	0.0080	1180	1350	57	12	
MS1500-Ezn-3	NaCl	-950	0.0080	1320	1496	36	41	Shear fracture accompanied by some amount of necking.
MS1300-E-30	NaCl	-1050	0.080	1105	1296	58	11	
MS1300-E-3	NaCl	-1050	0.0080	1085	1298	34	48	Shear fracture accompanied by some amount of necking.
MS1500-E-30	NaCl	-1050	0.080	1260	1490	53	13	Ductile; necking and cup-cone fracture, but with shallow surface fractures in the neck.

MS1500-E-3	NaCl	-1050	0.0080	1240	1526	13	79	Sharp shear fracture without necking. Surface fractures found near fracture lip.

Table 3 D_{eff} and C_H for MS1300 and MS1500 obtained from decay and rise transients in the permeation experiments. The solutions in the entry cell and exit cell consisted of 3.5 wt% NaCl and 0.1 M NaOH, respectively.

Specimen	Applied potential, $mV_{Ag/AgCl}$	Thickness, mm	i_{∞}, μA cm^{-2}	D_{eff}, $cm^2\ s^{-1}$	C_H, ug g^{-1}
MS1300	Start at -1050	1.13	1.40		0.137
	-950 (decay)		0.84	13.0×10^{-7}	0.082
	-850 (decay)		0.24	15.5×10^{-7}	0.024
	-950 (rise)		0.51	12.0×10^{-7}	0.049
	-1050 (rise)		0.73	8.8×10^{-7}	0.070
				Ave: $12.3 \times$	
MS1500	Start at -1050	1.09	1.09		0.115
	-950 (decay)		0.43	13.0×10^{-7}	0.046
	-850 (decay)		0.13	15.0×10^{-7}	0.014
	-950 (rise)		0.51	15.5×10^{-7}	0.054
	-1050 (rise)		0.73	9.2×10^{-7}	0.077
				Ave: $13.2 \times$	

Table 4 LIST results for MS1500 steel in (i) air, (ii) acidified 3.5 wt% NaCl, and (iii) 0.1 M HCl solution, at the open circuit potential, E_{corr}. The applied stress rate was 0.080 MPa s^{-1}. Unless otherwise noted in 'Remarks', fractures were ductile, accompanied by necking and cup-cone fracture, and MVC dimples present on fracture surface. n/a means not applicable.

Specimen designation	Environment	Threshold yield stress, σ_{TH}, MPa (±5)	Fracture or UTS, σ_f, MPa (±2)	Reduction in area, R_A, %	Hydrogen embrittlement index, I	Remarks
MS1500-A	Air	1275	1470	61	n/a	
MS1500-S-pH1	3.5 wt% NaCl	1070	1266	10	84	Sharp shear fracture without necking.
MS1500-S-pH3	3.5wt% NaCl	1210	1340	45	26	Mixed shear-ductile fracture with some amount of necking. Surface cracks in the neck area.
MS1500-S-pH5	3.5wt% NaCl	1220	1422	55	10	Cup-cone fracture with necking but with some surface cracks in the neck area.
MS1500-S-pH7	3.5wt% NaCl	1265	1430	60	2	
MS1500-S-pH9	3.5wt% NaCl	1240	1476	56	8	
MS1500-pH1	0.1 M HCl	1090	1270	28	54	Sharp shear fracture with small amount of necking. Small surface cracks near fracture lip.

Table 5 Tensile test results for different MS-AHSS in (i) air, (ii) 0.1 M NaOH, and (iii) 3.5wt% NaCl. The applied strain rate was 0.015 mm/mm/min. Unless otherwise noted in 'Remarks', fractures were ductile, accompanied by necking and cup-cone fracture, and MVC dimples present on fracture surface. n/a means not applicable. *Potential was measured versus Ag/AgCl/sat KCl.

Specimen designation	Environment	Potential, $mV_{Hg/HgO}$	Yield stress, σ_y MPa (±5)	Fracture stress, UTS, σ_f, MPa (±2)	Reduction in area, R_A, %	Hydrogen embrittlement index, I	Remarks
MS980-A	Air	n/a	895	1105	72	n/a	
MS980-H1100	0.1 M NaOH	-1100	910	1160	67	6	Cup-cone fracture with some cracks in the neck region.
MS980-H1400	0.1 M NaOH	-1400	900	1090	41	42	Cup-cone fracture with brittle features at the core. Some cracks in the neck area.
MS980-H1700	0.1 M NaOH	-1700	890	1130	40	43	Shear fracture with some amount of necking.
MS1180-A	Air	n/a	1170	1310	70	n/a	
MS1180-H1100	0.1 M NaOH	-1100	1190	1375	65	7	Cup-cone fracture with some cracks in the neck region.
MS1180-H1400	0.1 M NaOH	-1400	1190	1360	40	42	Cup-cone fracture with brittle features at the core. Some cracks in the neck area.
MS1180-H1700	0.1 M NaOH	-1700	1180	1370	36	49	Shear fracture with some amount of necking.
MS1300-A	Air	n/a	1190	1370	63	n/a	
MS1300-H1100	0.1 M NaOH	-1100	1200	1400	60	5	Cup-cone fracture with some cracks in the neck region.
MS1300-H1400	0.1 M NaOH	-1400	1185	1395	34	47	Cup-cone fracture with brittle features at the core. Some cracks in the neck area.
MS1300-H1700	0.1 M NaOH	-1700	1170	1405	31	50	Shear fracture with some amount of necking.
MS1500-A	Air	n/a	1340	1525	55	n/a	
MS1500-H1100	0.1 M NaOH	-1100	1350	1565	53	5	Cup-cone fracture with some cracks in the neck region.
MS1500-H1400	0.1 M NaOH	-1400	1335	1535	27	51	Shear fracture with some amount of necking; surface cracks near fracture lip.
MS1500-H1700	0.1 M NaOH	-1700	1205	1440	26	52	Shear fracture with little necking.

MS980-Ezn	3.5wt% NaCl	-950*	900	1125	71	0
MS1180-Ezn	3.5wt% NaCl	-950*	1190	1330	69	0
MS1300-Ezn	3.5wt% NaCl	-950*	1185	1355	63	0
MS1500-Ezn	3.5wt% NaCl	-950*	1585	1585	56	0